RICE UNIVERSITY

Dynamic Franz-Keldysh Effect and Its Applications
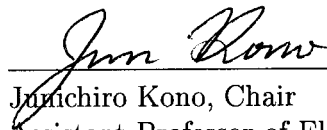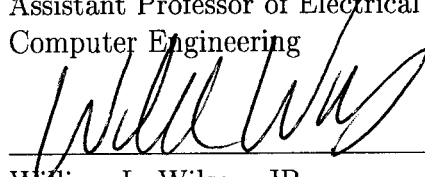
by

Ajit Srivastava

A Thesis Submitted
in Partial Fulfillment of the
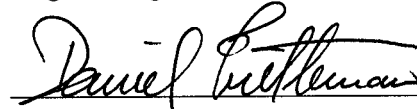Requirements for the Degree

Master of Science

Approved, Thesis Committee:

_____
Junichiro Kono, Chair
Assistant Professor of Electrical and
Computer Engineering

_____
William L. Wilson, JR.
Professor of Electrical and Computer
Engineering

_____
Daniel Mittleman
Assistant Professor of Electrical and
Computer Engineering

Houston, Texas

April, 2003

UMI Number: 1414299

UMI®

UMI Microform 1414299

ABSTRACT

Dynamic Franz-Keldysh Effect

and Its Applications

by

Ajit Srivastava

In this dissertation we study the dynamic Franz-Keldysh effect (DFKE) in GaAs. We observe the salient features of DFKE viz., below bandgap absorption and oscillations above the band gap, in our experiments. We also report the first observation of a large photoinduced transparency which represents a novel coherent phenomenon based on the DFKE and agrees well with the theoretical predictions. Finally we propose schemes making use of this effect to realize all-optical wavelength conversion required in high speed optical networks based on wavelength division multiplexing (WDM).

Acknowledgments

Contents

Illustrations

Chapter 1

Introduction

Solids under intense laser fields exhibit phenomena that cannot be understood by treating the field as a small perturbation. The interplay of spatially periodic lattice potential and the temporally periodic electric field of the laser leads to new and interesting physics. Depending upon the relative strength of the electric field and the photon energy of the laser beam, many fascinating effects have been predicted. The dynamic Franz-Keldysh effect (DFKE) is one such effect which causes observable changes in the absorption spectra near the fundamental band edge of a semiconductor. More precisely, it causes absorption of light even below the fundamental absorption edge and oscillations in the absorption spectra above the band edge [1]. With the advent of ultrafast femtosecond lasers, high intensities which are needed to see such effects are achievable in labs. Ultrafast changes induced by the intense laser can be studied using pump-probe spectroscopy. In this project, we were motivated to study these features of the DFKE experimentally, verify the predictions made by existing theories and consider its real-world applications.

1.1 Outline

In the next chapter, we review the effect of applied electric field on the optical properties of a semiconductor. We first discuss the ordinary (or dc) Franz-Keldysh effect, reviewing both theoretical and experimental work already done on these effects. Chapter 3 deals with the DFKE, which is a high frequency analog of the Franz-

Keldysh effect. We also study more general aspects of the changes brought about in the optical properties of a solid due to intense laser fields. In Chapter 4, we discuss our experimental setup in detail, covering the main components required for our experiment. Our experimental results and their interpretation are presented in the next chapter. We propose schemes for realizing all-optical switching based on the DFKE in Chapter 6. Finally, in Chapter 7 we sum up our work and discuss the scope for future study.

Chapter 2

Background and Literature Review: Electrooptics

The interrelation between electric field and optical phenomena presents a large variety of facets and diversity of applications. In this chapter we review various effects which arise due to the application of electric fields on semiconductors. We also consider the case of quantum confined semiconductors, where excitonic effects are more important. We first look at the changes brought about by the electric field well below the fundamental absorption edge. However, when the light frequency is very close to those of electronic transitions, more complex dependences of n on the electric field have to be considered, which are markedly dependent on the specific physical mechanisms.

2.1 Changes in the transparent region

Here we talk about changes in the transparent region of a semiconductor due to an applied electric field. The electric field-induced change Δn in the real refractive index, *electrorefraction*, provides a physical method to modify in a controllable way the phase, the direction and the polarization of a light beam. On the other hand, the electric field-induced change $\Delta \kappa$ in the imaginary part, *electroabsorption*, permits the direct control of the light intensity passing through the material. The external electric field could either be a dc electric field or a low-frequency ac field or could even be the electric field of a strong laser. If the change in refractive index depends linearly on the strength of the applied electric field, the change is known as the linear electrooptic, or *Pockels*, effect. The linear electrooptic effect can be described in terms of a nonlinear

polarization given by [2]

$$P_i(\omega) = 2 \sum_{jk} \chi_{ijk}^{(2)}(\omega = \omega + 0) E_j(\omega) E_k(0). \qquad (2.1)$$

Since the linear electrooptic effect can be described by a second-order nonlinear susceptibility, it implies that the Pockels effect can only occur for materials that do not exhibit inversion symmetry. In materials which exhibit inversion symmetry, the lowest-order change in the refractive index depends quadratically on the applied electric field. This effect is known as the *Kerr* effect or as the quadratic electrooptic effect. It can be described in terms of a nonlinear polarization given by

$$P_i(\omega) = 3 \sum_{jkl} \chi_{ijkl}^{(3)}(\omega = \omega + 0 + 0) E_j(\omega) E_k(0) E_l(0). \qquad (2.2)$$

One may expand $\Delta(1/n^2)$ in powers of $\mathbf{E}$ and so that up to the second order one can write [3]

$$\Delta(1/n^2)_{ij} = r_{ijk} E_k + s_{ijkl} E_k E_l. \qquad (2.3)$$

The linear term determines the Pockels effect whereas the quadratic term is responsible for the Kerr effect. The corresponding linear and quadratic electrooptic coefficients r_{ijk} and s_{ijkl} constitute third- and fourth-rank tensors, respectively, whose components depend on the light frequency ω due to material dispersion. Moreover, in most experiments the applied field $\mathbf{E}$ is modulated at a certain frequency Ω. The Pockels effect can be used to modulate the polarization and intensity of light beam. Pockel devices based on $LiNbO_3$, $LiTaO_3$, KDP have found widespread use. The Optical Kerr effect, on the other hand, can be used to vary refractive index with intensity and finds application in self-focussing of a gaussian beam.

2.2 Near band edge changes

Much more interesting changes in the electroabsorption are observed near the optical band gap of the semiconductor.

Bulk semiconductor

Let us first consider a bulk semiconductor at room temperature where we talk of free carrier electroabsorption. Franz and Keldysh, almost forty year ago, independently proposed the existence of an electric-field dependent absorption *tail* below the band gap and oscillations in the absorption spectra above the band gap for the bulk case. The application of a dc electric field **F** results in the addition of the potential energy term $-e\mathbf{F} \cdot \mathbf{r}$ to the electron Hamiltonian and thus the translational symmetry is lost in the direction of the applied electric field. This gives rise to penetration of valence and conduction wave functions into the bang gap and leads to photon-assisted tunneling of electrons from valence to conduction band. To treat the Franz-Keldysh effect, we have to solve the effective-mass Schrödinger equation for an electron-hole pair in a static electric field, neglecting the electron-hole Coulomb interaction (i.e., no exciton effects). This assumption decouples the motion in the direction of the field (say the z direction) from that in the other coordinate directions, leaving those motions as plane waves, and the only non-trivial equation that remains to be solved is for the relative motion in the direction of the field, giving

$$\left(-\frac{1}{2m}\frac{\partial^2}{\partial z^2} + eFz \right) \phi(z) = E\phi(z) \tag{2.4}$$

where $z = z_e - z_h$, F is the electric field, m is the reduced effective mass of the electron and ϕ is the envelope part of the total wavefunction in the z - direction. This equation may be solved exactly [4], giving a continuous spectrum of energies with Airy functions as the wavefunctions (see Fig. 2.1 [5]), and an explicit formula
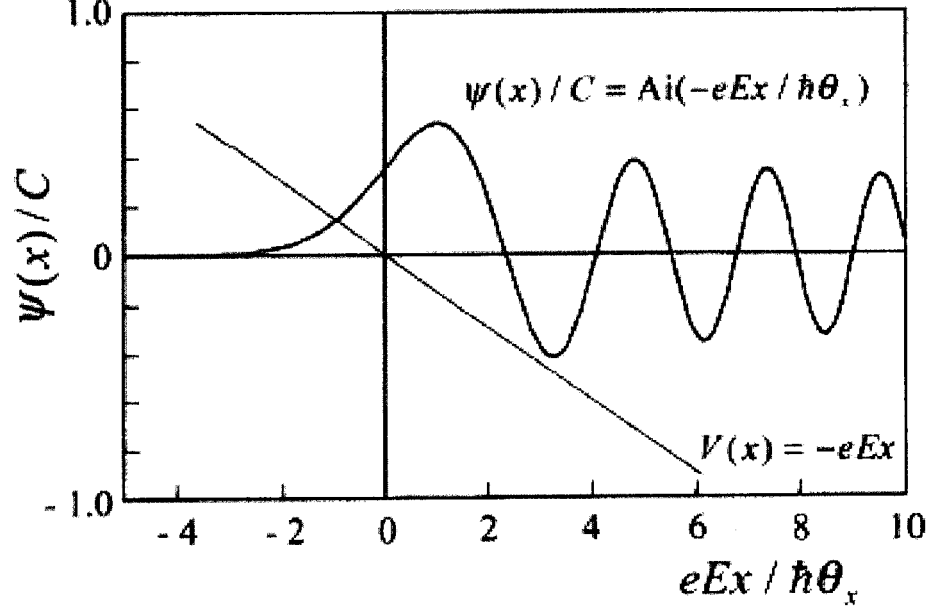
Figure 2.1 : Wavefunction of an electron-hole pair in a static electric field, with a tilted potential barrier. The wavefunction penetrates into the region $E < -eFz$ [5].

can be obtained for the Franz-Keldysh absorption. The total absorption spectrum is found to be

$$\alpha(\omega) = \frac{\alpha_b}{2\pi} \frac{mf^{1/3}}{\hbar^2} \left(-\epsilon Ai^2(\epsilon) + [Ai'(\epsilon)]^2 \right) \tag{2.5}$$

where

$$\alpha_b = \frac{8\pi^2 |d_{cv}|^2 \omega}{nc}, \quad f = eF \frac{2m}{\hbar^2} \tag{2.6}$$

d_{cv} and n being the interband dipole matrix element and the refractive index respectively.

Fig. 2.2 [4] shows the resulting absorption as a function of $\epsilon = E_g - \hbar\omega$. Due to the oscillatory character of the Airy functions for negative arguments, one gets oscillations in the absorption spectrum above the band gap. The amplitude of oscillations
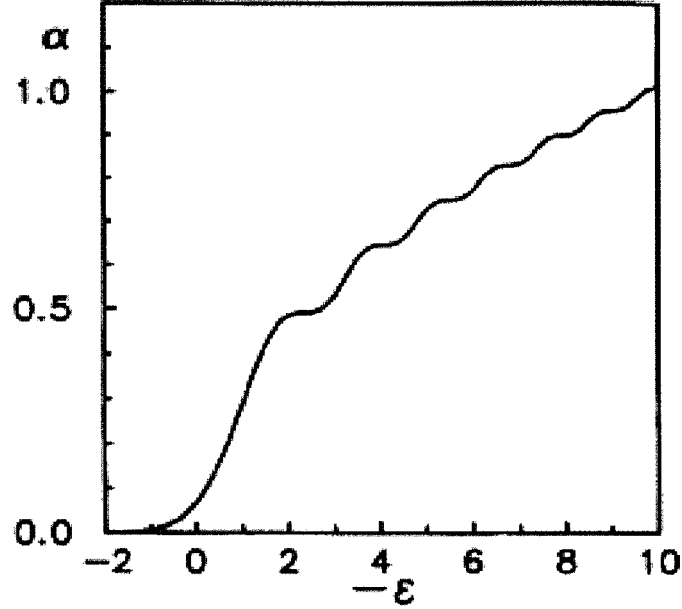
Figure 2.2 : Absorption α plotted against ϵ [4].

decreases with increasing energy. One can also see from Fig. 2.2 that the absorption has a tail below the gap, i.e., for $\hbar\omega < E_g$ or $\epsilon > 0$. Using the asymptotic form of Airy function [4], we obtain the below-gap absorption as

$$\alpha(\omega) = \frac{\alpha_b}{32\pi^2} \frac{f}{E_g - \hbar\omega} \exp\left(-\frac{4}{3f}\left(\frac{2m(E_g - \hbar\omega)}{\hbar^2}\right)^{3/2}\right). \tag{2.7}$$

The above expression describes the exponential low energy absorption tail which is caused by the applied electric field. As mentioned earlier, this may be understood as a photon-assisted field-induced tunneling of an electron from the valence into the conduction band, as is illustrated in Fig. 2.3 [3]. The oscillations above the band gap can possibly be due to the change in overlap integrals of wavefunctions and the relaxation of selection rules caused by the lowering of the translational symmetry of

C. B.

V. B.

E = 0

E ≠ 0
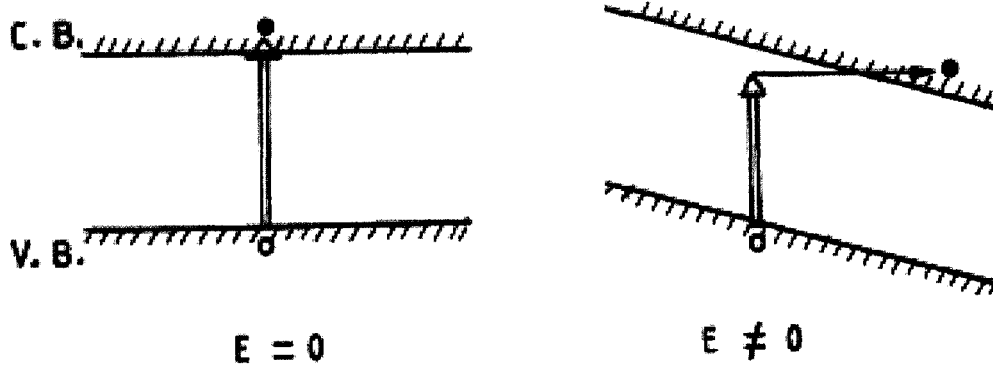
Figure 2.3 : Illustration of the Franz-Keldysh effect. Application of a field tilts the bands and permits tunneling from an excited virtual band to the conduction band [3].

the system.

The absorption spectrum far above the band edge, $\hbar\omega >> E_g$ can be estimated by taking proper limits [4] with the result

$$\alpha(\omega) = \frac{\alpha_b}{4\pi^2} \left(\frac{2m}{\hbar^2}\right)^{3/2} \sqrt{\hbar\omega - E_g} \tag{2.8}$$

which is the well-known expression for absorption in a $3d$ system.

The change in absorption coefficient in an electric field is quite small and even an available high electric field such as ($\leq 10^5 V/cm$) will give rise to a change of a small fraction. Therefore, it is very difficult to observe the exponential tail and oscillatory behavior of the absorption. However, applying a periodically oscillating field and using a phase-sensitive detector (lock-in amplifier), the change in absorption coefficient can be measured with high accuracy. This method is often referred to as *electroreflectance* or *electroabsorption* and has been applied to study the optical properties of semiconductors in the region from the ultraviolet to the infrared since the 1960s. The method is also called *modulation spectroscopy*, including many other
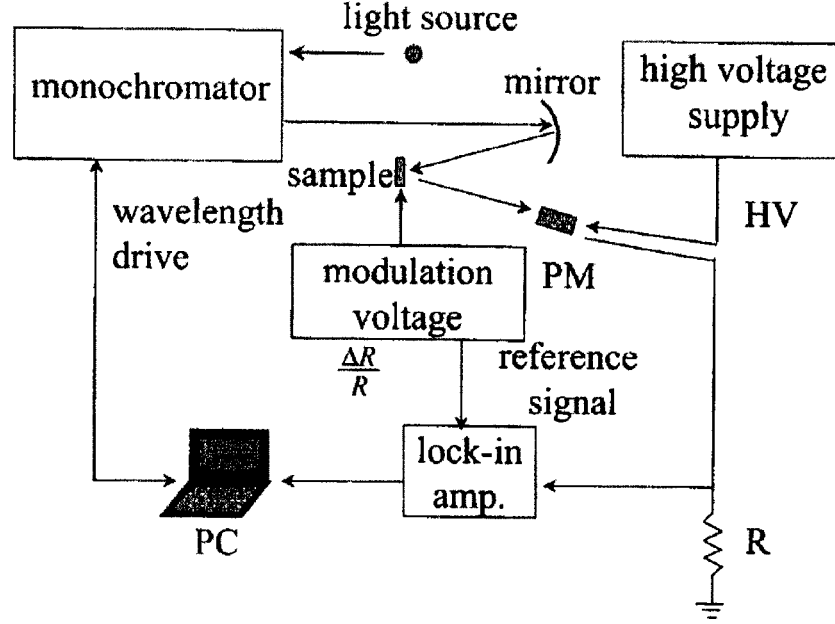
Figure 2.4 : Experimental setup for modulation spectroscopy [5].

modulation methods such as stress modulation and magnetic field modulation. In general, modulation spectroscopy is carried out by using the experimental setup as shown in Fig. 2.4 [5].

Electroreflectance and electroabsorption measurements have been extensively used to probe both direct and indirect edges in various semiconductors [6]. Fig. 2.5 [7] shows one such study done on In-Sn-O/InP semiconductor [7]. The peaks labeled $D - O$ are the Franz-Keldysh oscillations.

2.2.1 Quantum Wells

Quantum well (QW) electroabsorption differs from that of bulk in several ways, most importantly, the mechanism is very different depending on whether the electric field
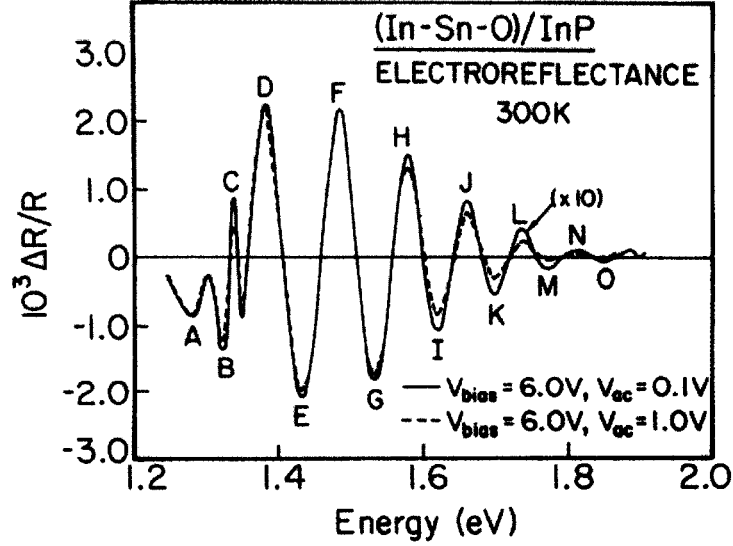
Figure 2.5 : Experimental electroreflectance spectra for different voltages showing Franz-Keldysh oscillations above the band edge [7].

is parallel or perpendicular to the QW layers. Also in QWs, the Coulomb interaction between the electron-hole pair (exciton) needs to be considered. If one applies the electric field perpendicular to the layer of a quantum well, the situation is qualitatively different from that in bulk material. Because of the opposite charges, the field pushes the electrons and holes toward the opposite walls of the well. Hence, the overlap between the corresponding particle-in-a-box envelope is modified. We first neglect the electron-hole Coulomb interaction. This model, for reasons that will become obvious later, is called the *quantum-confined Franz-Keldysh effect* (QCFKE) [8]. Let us consider, for simplicity, a potential well of infinite depth extending over $-L/2 \leq z \leq L/2$. Within the envelope function approximation, the pair wavefunction of a narrow quantum well can be taken as the product of particle-in-a-box envelope for the electron and hole times the function describing the relative motion in the plane

of the layer

$$\psi_\mu(\mathbf{R}, \mathbf{r}) = \psi_{n_e}(z_e)\psi_{n_h}(z_h)\phi_{k_\parallel}(\mathbf{r}_\parallel). \tag{2.9}$$

Electron and hole wavefunctions in the z direction obey the equation

$$\left(-\frac{\hbar^2}{2m_i}\frac{d^2}{dz_i^2} \pm eEz_i\right)\psi_{n_i}(z_i) = E_{n_i}\psi_{n_i}(z_i) \tag{2.10}$$

where the $+$ (-) sign is linked to $i = e(h)$. The boundary conditions are

$$\psi_{n_i}(z = \pm L/2) = 0 \tag{2.11}$$

As can be seen easily, the above equations are similar to the bulk case and hence the solutions are again Airy functions. Fig. 2.6 [8] illustrates the calculated wavefunctions in the potential well with and without an electric field. It must be noted that for the zero-field case, only $n_c = n_v$ transitions are allowed. Fig. 2.7 [8] shows the calculated absorption spectrum for a GaAs quantum well with L = 150 Åwidth in the presence of an electric field of 10^5 V/cm. It is clear from Fig. 2.6 and Fig. 2.7 that overlap integral between the valence and conduction band states changes due to the field. Another very important point that is clear from Fig. 2.7 is that the 'forbidden' transitions ($n_c \neq n_v$) are becoming strong. This is simply because the electron and hole wavefunctions are no longer sinusoidal and all the overlap integrals are in general non-zero. Perhaps, the most fascinating observation is that for the limit $L \rightarrow \infty$, the inter-subband transitions approach the modulation of the bulk Franz-Keldysh spectrum. As the thickness of the well is increased at a fixed field, one sees a smooth transition from a strongly quantized behavior at small thickness that bears little relation to the Franz-Keldysh effect, to the Franz-Keldysh - like behavior. This simple model can elegantly explain the Franz-Keldysh oscillations above the band gap. For photon energies below the band gap, the overlap of the electron
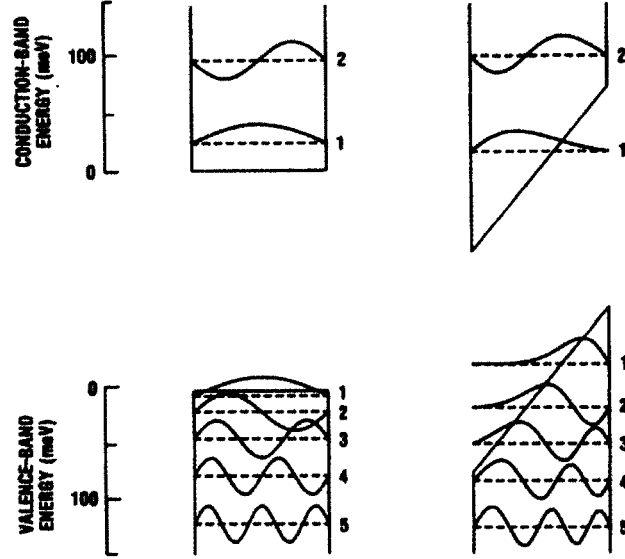
Figure 2.6 : Calculated wavefuntions and energy levels for a QW with and without an applied electric field [8].

and hole Airy functions is such that the oscillatory tail of one function overlaps the exponential tail of the other; as the photon energy is varied, there is no oscillatory behavior in the overlap. However, for photon energies above the band gap, $E_e + E_h$ is positive and there is a region of overlap of the oscillatory tails. Varying this overlap results in the Franz-Keldysh oscillations of the total overlap integral and hence the optical absorption.

The above model of QCFK effect was pedagogically important but it was too simple in that it neglected even the Coulomb interaction between the electron-hole pair. When the effect of Coulomb correlations of electron and hole is properly included a Stark shift of exciton resonance to lower energies is expected [9]. This Stark shift is intuitive if we go back to the hydrogenic-atom picture. With the application of an electric field, the symmetry of the atom is reduced and degeneracy between the
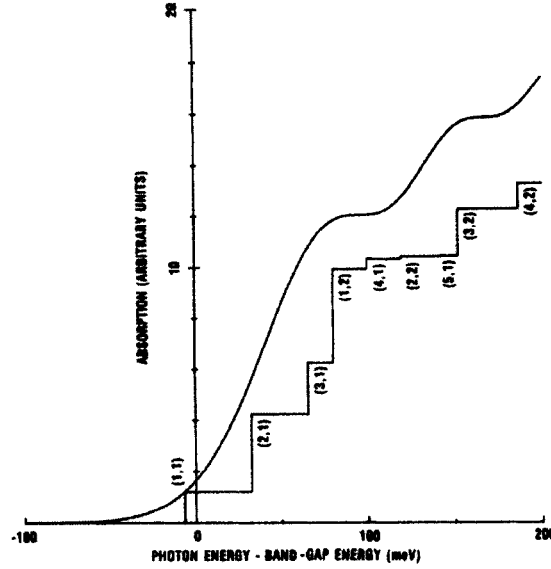
Figure 2.7 : Calculated absorption of a QW, in presence of an electric field perpendicular to the QW plane, neglecting the excitonic contributions [8].

levels is lifted giving rise to the Stark effect. An excitonic system is very similar to a hydrogenic-atom and hence one expects similar observations. However, for fields of the order of a few times the classical ionization field E_i ($= E_B/8ea$, where E_B is the zero-field binding energy and a is the Bohr radius), the resonance is broadened because field ionization drastically reduces the excitonic lifetime. In GaAs-AlGaAs quantum wells, however, large shifts in band-edge absorption are observed [10]. These shifts can exceed the exciton binding energy and yet the exciton resonances remain well resolved. To explain this seemingly anomalous behavior, we note that the electric fields perpendicular to the QW layers pull the electrons and holes towards opposite sides of the layers resulting in an overall net reduction in energy of an electron-hole pair and a corresponding Stark shift in the excitonic absorption. Also the walls of the quantum well impede the electron and hole from tunneling out of the well in rapid field
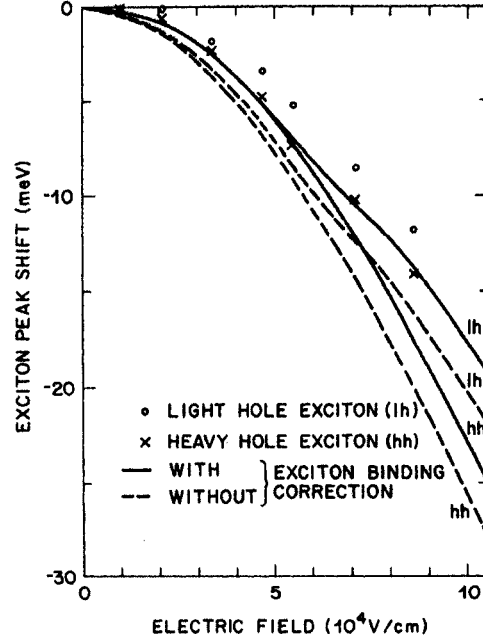
Figure 2.8 : Quantum-confined shift of the exciton peak position with applied field [10].

ionization. Because the well is narrow compared to the 3D excitonic size, electron-hole interaction, although slightly weakened by the separation of electron and hole, is still strong, and well defined excitonic states can still exist. Thus exciton resonances can remain to much higher fields than would be possible in the absence of this confinement, and large absorption shifts can be seen without excessive broadening. This mechanism is often referred to as the *quantum-confined Stark effect* (QCSE) [10]. Fig. 2.8 [10] shows experimentally observed exciton peak position vs. applied field.

There has been a report of observation of Franz-Keldysh oscillations in QW systems [11]. The authors measure photocurrent spectra of a single InGaAs QW in electric fields perpendicular to the growth direction. As shown in Fig. 2.9 [11], oscillations are resolved in modulation spectra. If we consider the excitonic picture then
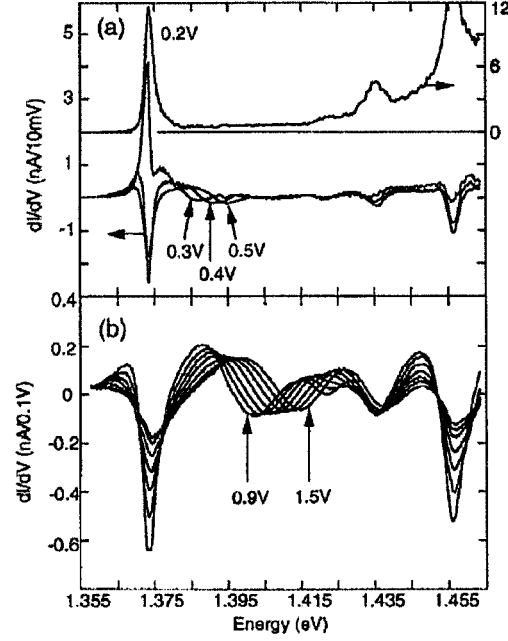
Figure 2.9 : Franz-Keldysh types oscillations observed in photocurrent spectra of InGaAs QW [11].

we expect to see a QCSE kind of shift in the exciton spectrum. However, from Fig. 2.9 it is clear that the data resembles the bulk case much more than the QCSE as it is devoid of any excitonic peaks. Hence the authors conclude that the electric field in their system is strong enough to ionize the exciton, thereby leading to a bulk FK type effect which is due to the free carriers. What is unclear here is whether the Franz-Keldysh effect is present, but masked due the excitonic peak, before the ionization of the exciton or does it manifest itself only after the ionization of the exciton.

Chapter 3

High Frequency Effects and the Dynamic Franz-Keldysh Effect

In the previous chapter we considered the effect of a static electric field on the optical properties of a semiconductor. We saw that interesting effects arise near the fundamental absorption edge due to the applied electric field. In this chapter we consider the behavior of a semiconductor which is subjected to *strong ac* electric fields. Such strong ac fields can be generated by present day lasers. In section 3.1, we discuss the optical Stark effect which is essentially a resonant effect but includes response at arbitrary field intensities and not just weak fields. Extremely strong laser fields can not be treated as perturbation to the crystal Hamiltonian and novel effects are expected for solids in such a regime. We review some literature relating to this regime in section 3.2. Finally, in section 3.3 we discuss the dynamic Franz-Keldysh effect which is the high frequency analog of the Franz-Keldysh effect.

3.1 Optical Stark Effect

In recent years it has been discovered that optical response of direct-gap semiconductors shows some similarities to that of atomic systems if the time scales involved are shorter than characteristics equilibrium times of the semiconductor electron-hole excitations. These conditions are best met for the pump-probe spectroscopy with ultrashort laser pulses. The atomic counterpart of the optical Stark effect has been extensively studied. Here the coherent light field mixes the wavefunctions of the two

states leading to the *dressed states*. Even though this Stark effect is well-known in atomic systems, it has been observed only recently in semiconductors since the dephasing times are very short. We discuss the case of nonresonant excitation of exciton, where it is a good approximation to ignore absorption and generation of real carriers. It must be noted here that the optical Stark effect (OSE) is essentially resonant compared to the dynamic Franz-Keldysh effect (DFKE) which we discuss later. In the OSE we only consider relatively small detuning values as opposed to the DFKE. To formally understand the theory of OSE, one needs to resort to the semiconductor Bloch equations [4]. We do not attempt such a detailed derivation here but explain the salient features of OSE in a qualitative way. A coherent pump field falling in the transparent region of the medium is used to *dress* the excitonic states. Consider the crystal ground state $|0, n\rangle$ is energetically nearly degenerate with the state $|x, n - 1\rangle$ where one photon is removed and one exciton is created. A similar situation holds for states $|0, n + 1\rangle$ and $|x, n\rangle$ and so on. Applying exciton-radiation-field interaction [12] between nearly degenerate states leads to new mixed eigenstates (as shown in Fig. 3.1 [12]) α_n, β_n; α_{n+1}, β_{n+1}; etc, which are split by the quantity

$$\hbar\Delta = \hbar[(\omega - \omega_0)^2 + \Omega^2]^{1/2}, \tag{3.1}$$

where $\omega - \omega_0$ is the detuning of the pump laser freuency ω from the exciton resonance at ω_0, and Ω is the Rabi frequency

$$\hbar\Omega = p_{0x}|E| \tag{3.2}$$

with p_{0x} being the effective matrix element between the ground and exciton states.

From Fig. 3.1 we see that the exciton resonance is blue-shifted by $\hbar\Delta$. This is the case for negative detuning ($\omega - \omega_0 < 0$). A red shift of the levels is expected for positive detunings. Fig. 3.2 shows a calculation of such a shift for different pump intensities in a GaAs QW [4].
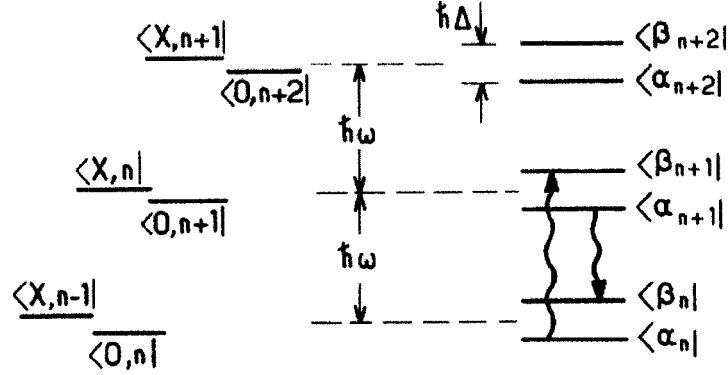
Figure 3.1 : Schematic representation of relevant energy levels without (left) and with exciton phonon interaction (right) [12].

Such a shift has experimentally been observed in GaAs-AlGaAs multiple QWs by [12] for the nonresonant pump case. Fig. 3.3 shows a blue shift of exciton during the presence of the pump pulse [12]. The fact that the sample returns to its original state after the end of the excitation shows that no population of excitons or real carriers has been generated by the pump pulse. The magnitude of the shift in excitonic resonance is comparable to that predicted by the theory.

3.2   Solids in intense laser fields

Matter in the presence of an ac electric field of sufficient strength exhibits phenomena that cannot be understood by treating the field as a small perturbation. As we saw in the previous section, the OSE, which occurs in the presence of strong driving fields nearly resonant with electronic transitions, is better described by coupled light-matter states or dressed states than by perturbation theory. Such high intensity $(10^{14} \ W/cm^2)$ can now be achieved using ultrashort femtosecond laser pulses. One way to characterize high intensity in the realm of quantum mechanics is to consider
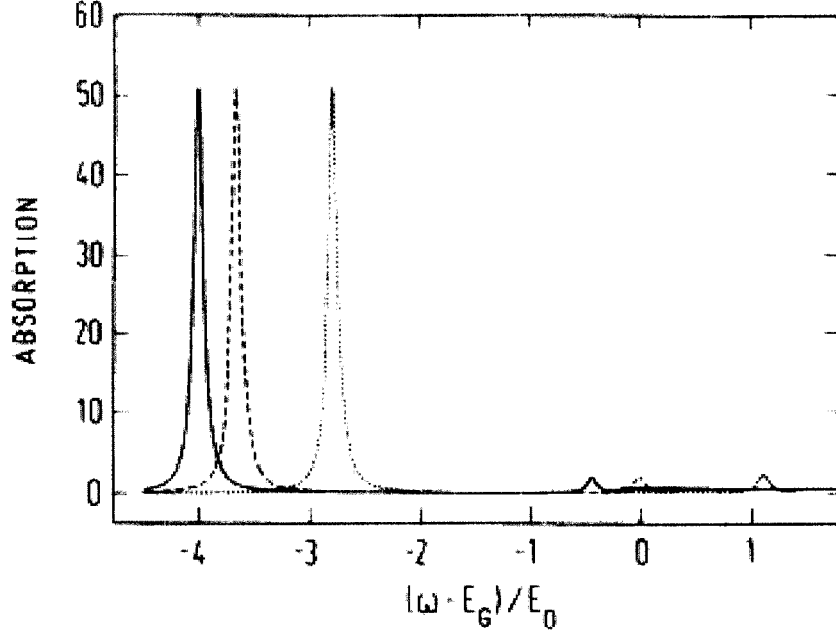
Figure 3.2 : Calculated 2d absorption spectrum for pump intensities $I_p = 0$ (solid line), 7.5 MW/cm^2 (dashed line), and 30 MW/cm^2 (dotted line), showing the optical Stark shifts of the exciton resonance in a GaAs QW [4].

the photon density of laser beam. When the photon density exceeds one per cubic wavelength, the field can be considered as classical. Indeed the present day ultrafast lasers are intense in this sense. It is this transition between quantum and classical energy scales that leads to new phenomena in solids at these intensities.

To quantify such an energy scale we consider a free electron in a strong laser field. Since the electric field is oscillating rapidly, it imparts a wiggling motion to any charged particle in its path. The time averaged kinetic energy of wiggling is known as the *ponderomotive energy* of the classical particle [13]. The vector potential for an electromagnetic field polarized along $\hat{\epsilon}$ and propagating along $\hat{z}$ may be written as

$$\mathbf{A} = A_0(\mathbf{x}, t)\hat{\epsilon}\sin(kz - \omega t) \tag{3.3}$$
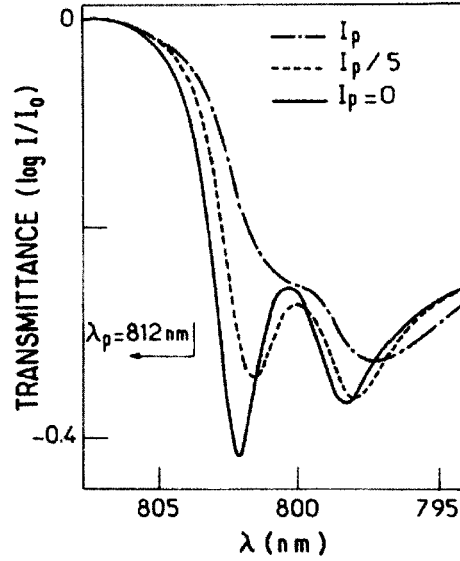
Figure 3.3 : Transmission spectra of a MQW at 15 K showing a blue shift of the excitonic resonance due the optical Stark effect [12].

The Hamiltonian of an electron in the electromagnetic field is

$$H = \frac{[\mathbf{p} - \frac{e}{c}\mathbf{A}(\mathbf{x}, t)]^2}{2m} \tag{3.4}$$

Using the adiabatic approximation, we average the Hamiltonian over one laser period to get

$$\langle H \rangle = \frac{p^2}{2m} + \frac{e^2 A_0^2(\mathbf{x}, t)}{4mc^2} = T + U_p \tag{3.5}$$

The second term on the right hand side is the average energy due to wiggling. It appears in the Hamiltonian as a positive-definite scalar function of position and time, and hence acts as an effective potential energy, known as the ponderomotive potential. This is the relevant energy scale which distinguishes classical and quantum regime. If the photon energy is much larger than the ponderomotive potential,

$$\hbar\omega \gg U_p$$

we have the quantum regime and treat light as photons. On the other hand, if the ponderomotive potential is much larger than the photon energy,

$$\hbar\omega << U_p$$

we essentially have the classical regime and consider the electric field picture. One expects to see novel phenomena when the two parameters are comparable to each other, as we shall later.

As a simple but illustrative example, let us first quantitatively understand what happens to an electron in intense light. As mentioned earlier, we cannot treat such intense light as a perturbation. The Schrödinger equation for a free spinless electron in the presence of light using the $\mathbf{A} \cdot \mathbf{p}$ is

$$\frac{[\mathbf{p} - \frac{e}{c}\mathbf{A}(\mathbf{x}, t)]^2}{2m}\psi(\mathbf{x}, t) = i\hbar\frac{\partial\psi(\mathbf{x}, t)}{\partial t}. \tag{3.6}$$

In the electric dipole approximation, the spatial dependence of the vector potential can be neglected. The solutions of (3.6), called Volkov states, are the quantum-mechanical analogs of free wiggling electrons. They are plane waves, with an oscillating phase, modulated by the electromagnetic vector potential:

$$\begin{aligned}
\psi_{Volkov}(\mathbf{x}, t) &= \exp\left[\frac{i}{\hbar}\left(\mathbf{p} \cdot \mathbf{x} - \frac{i}{\hbar}\frac{p^2}{2m}t - \frac{i}{\hbar}\frac{e^2 A_0^2}{4mc^2}t - \frac{i}{\hbar}\frac{e^2 A_0^2}{8\omega mc^2}\sin(2\omega t)\right.\right. \\
&\quad + \left.\left.\frac{i}{\hbar}|\hat{\epsilon} \cdot \mathbf{p}|\frac{eA_0}{m\omega c}\sin(\omega t)\right)\right]
\end{aligned} \tag{3.7}$$

The Volkov state is a superposition of plane wave energy eigenstates that are separated by integer multiples of $\hbar\omega$:

$$\begin{aligned}
\psi_{Volkov}(\mathbf{x}, t) &= exp\left[\left(\frac{i}{\hbar}(\mathbf{p} \cdot \mathbf{x} - \frac{p^2}{2m} - U_p)\right)\right] \\
&\quad \times \sum_{n=-\infty}^{\infty}\sum_{m=-\infty}^{\infty} J_m\left(\frac{e^2 A_0^2}{8\hbar\omega mc^2}\right) J_{n-2m}\left(|\hat{\epsilon} \cdot \mathbf{p}|\frac{eA_0}{\hbar\omega mc}\right) e^{in\omega t}
\end{aligned} \tag{3.8}$$

Here J_m's are cylindrical Bessel functions, whose arguments are the coefficients of the oscillating terms in the Volkov phase. We shall see later that in DFKE too similar Bessel function terms appear implying a non-perturbative treatment of the laser field. In fact, even for electrons in a semiconductor, if we use the effective mass approximation, replacing m by m^* should give us the required wavefunctions. As we see later, this is indeed the case. It is relevant to ask whether such an approximation holds good if the laser field is extremely intense. In such a case, the potential of lattice and the ponderomotive potential of the laser should be dealt on an equal footing. In the extreme case, the lattice potential may in fact be treated as a perturbation to the ponderomotive potential.

For the case of an electron in a spatially periodic potential without any applied time-varying electric fields, we have Bloch functions as the eigenstates of the Hamiltonian. When, instead of a spatially periodic potential, we have a temporally periodic potential, as may be the case for a charged particle in an ac field, the eigenstates are Floquet states which are the temporal analog of the Bloch states and are given by [14]

$$\psi_\alpha(t) = \exp(-\tilde{\epsilon}t/\hbar)\phi_\alpha(t) \tag{3.9}$$

Here $\tilde{\epsilon}$ is called the *quasienergy* of the electron which is an analog of the crystal momentum or the quasimomentum of the electron. As in the case of a spatially periodic potential, where the crystal momentum spectrum of the electron showed gaps, we expect to observe forbidden gaps in the quasienergy spectrum of electrons [15]

$$E = \frac{p^2}{2m} \pm |V_g J_n(gR_0)| \tag{3.10}$$

where V_g are the Fourier coefficients of the lattice potential, $R_0 = e\mathrm{E}_0/m\omega^2$, and $J_n(x)$ is a Bessel function with a real argument. The above expression introduces a

new length scale R_0, which is the amplitude of electron oscillation in the laser field. Thus, when R_0 is comparable to the lattice constant of the material a_0,

$$R_0 \simeq a_0,$$

there is a modulation of the band gap such that it produces a decrease of the band gap as the laser field strength increases. It should be noted here that this modulation of band gap, which depends on the intensity of the laser field, is particularly fascinating because it can be tuned to control the energy spectrum of a solid. An interesting connection between the relevant energy scale U_p and the relevant length scale R_0 can be made if we realize that the condition $U_p \simeq \hbar\omega$ is equivalent to the condition that

$$\omega \simeq \omega_B \tag{3.11}$$

where ω_B is the Bloch frequency given by

$$\omega_B = eEa_0/\hbar \tag{3.12}$$

Substituting $E = A_0\omega$ gives the equivalency. Thus this is an alternate way of looking at the condition for the DFKE.

3.3   Dynamic Franz-Keldysh effect

After a review of electrooptical effects and the effect of strong laser fields on solids, we discuss the DFKE in this section. It is the main subject of investigation of this thesis and following chapters will discuss our experimental work on the DFKE.

As the name implies DFKE is a direct dynamical analog of the FKE which we discussed in the previous chapter. One expects to see deviations from the dc behavior when the frequencies of the applied field are comparable to the frequencies at which carriers traverse the Brillouin zone (Bloch frequency [see Eq. (3.11)]). In DFKE, the

transmission of a probe beam near the band edge is modified in the presence of an intense laser beam much smaller in energy than the band gap. If we consider the very low frequency case, a beam of light transmitted through a sample on which an ac electric field is applied will be amplitude modulated because of the time variation of the absorption coefficient. A Fourier analysis of such a beam shows that in addition to the main frequency, there are sideband frequencies. For the high frequency case, the DFKE predicts increased sub-gap absorption and a blue shift of the main absorption edge, as well as non-linear mixing between the strong MIR pump and the probe beam producing optical sidebands.

Y. Yacoby theoretically calculated the transition rate due to a probe field of frequency Ω for a two-band model using time-dependent wavefunction which is a solution to the time-dependent Schrödinger equation with the high-frequency electromagnetic field of frequency ω included in the Hamiltonian [1]. It should be noted here that $\hbar\omega$ is much smaller than the band gap thus avoiding any creation of real carriers. On the other hand, $\hbar\Omega$ is taken to be close in size to the gap energy. Assuming parabolic conduction and valence bands gives the change in transition rate caused by the ω field which is shown in Fig. 3.4 [1] where,

$$A_{on} = \frac{eA_0}{(\hbar\omega m^*)^2} \propto (\frac{U_p}{\hbar\omega})^{1/2}. \tag{3.13}$$

It is worth mentioning here that the explicit expression for the transition rate contains J_ns just as we obtained for the case of solids in the presence of intense laser fields.

It is clear that DFKE falls in the regime

$$U_p \simeq \hbar\omega.$$

By taking the limit $A_{on} \to 0$ one obtains the average transition rate for a two-photon absorption. This is expected from our understanding of ponderomotive potential and
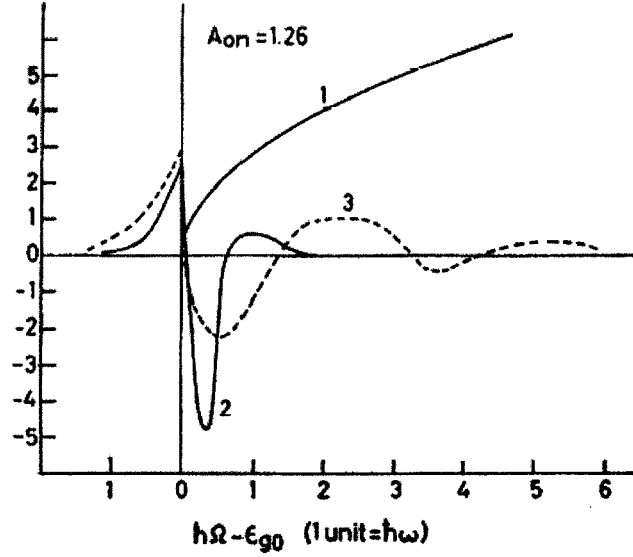
Figure 3.4 : Curve 1: The transition rate without the ω perturbation. Curve 2: The time average of the change in the transition rate caused by the ω. Curve 3: The time average of the change in the transition rate caused by an electric field $E_0 = 4 \times 10^4$ V/cm applied at very low frequency [1].

photon energy. As is seen from Fig. 3.4, there is a field-induced below band gap absorption and also oscillatory behavior above the gap. Though the blue-shift of band edge as predicted by [16] is not seen very clearly. One expects a blue-shift of band edge by an amount comparable to U_p because the wiggling electron now has this extra energy. Such a general behavior is also predicted in lower dimensional systems as is shown in Fig. 3.5 [16].

The theory also predicts appearance of only those sidebands which are an even number times ω away from the center frequency Ω ($\Omega \pm 2\eta\omega$), which is consistent with physical intuition: Since there is no preferred direction, it does not matter if the field direction is reversed, $\mathbf{E} \rightarrow -\mathbf{E}$, if the driven semiconductor possesses inversion symmetry.
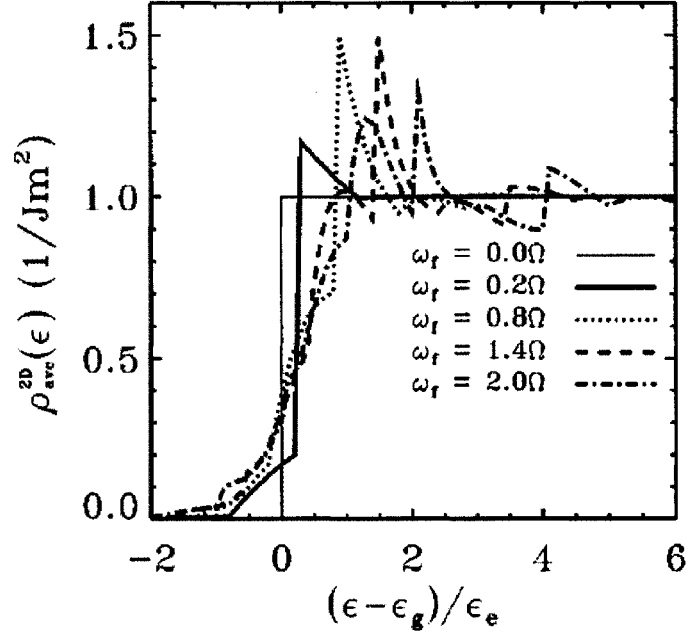
Figure 3.5 : DOS for a 2D system for different ratios of ponderomotive potential and photon energy [16].

Recently, there has been much interest in experimentally observing the DFKE. Chin *et al.* observed below band gap absorption in bulk GaAs by using intense femtosecond midinfrared (MIR) pulses (see Fig. 3.6) [17], while Nordstrom *et al.* could see a manifestation of DFKE in QWs. The latter observed a red shift of the exciton spectrum for THz frequencies smaller than the $1s \rightarrow 2p$ transition which they attributed to the optical Stark effect [18]. At higher intensities, the shift reversed its sign to a blue-shift which can be understood as a manifestation of the DFKE (see Fig. 3.7 [18]). The exciton peak could still be resolved at higher intensities ruling out the case of complete ionization of the exciton. Thus, their result can be understood as a competition between the DFKE and the OSE. There have also been reports on the observation of sidebands and generation of THz radiation by various groups
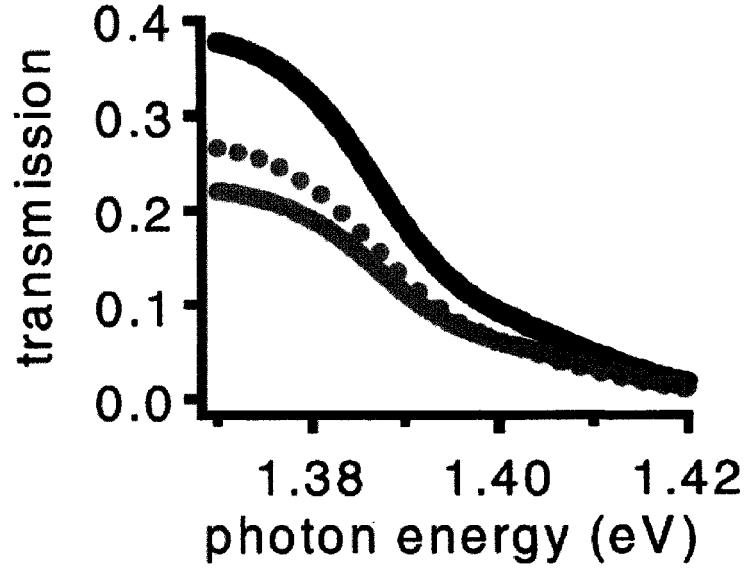
Figure 3.6 : Below bandgap absorption in bulk GaAs in presence of 3.5 μm pump laser due to the DFKE [17].

[19, 20, 21, 22].

The main features of the DFKE can be summarized as follows:

1. absorption below the band gap

2. oscillations in the absorption spectra above the band gap

3. blue-shift of the main absorption edge

4. generation of sidebands which are even harmonics of the pump frequency (if system has inversion symmetry)

5. most pronounced effect observed when $U_p \simeq \hbar\omega$

6. the effect on $U_p/\hbar\omega$, which predicts peculiar power and wavelength dependences. For example, the effect can be larger with smaller intensities if the wavelength
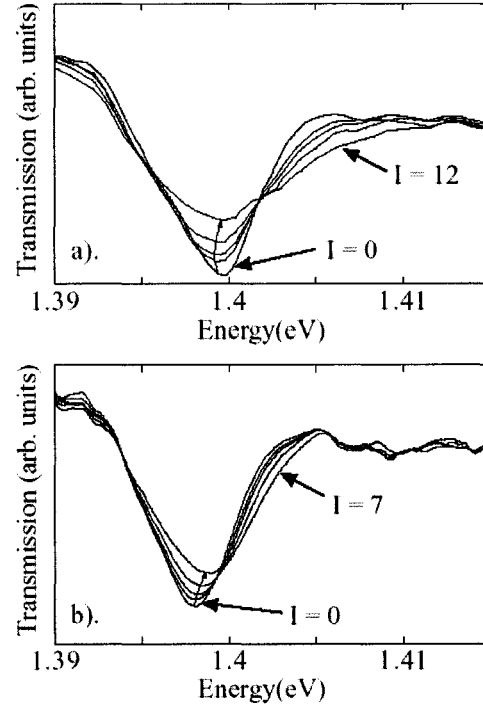
Figure 3.7 : Transmission spectra near exciton resonance with $\hbar\omega_{THz} = 2.5$ mev at different intensities [18].

is increased (as we observe in our experiments [see Chapter 5]).

Chapter 4

Experimental Methods

In this chapter we discuss our experimental setup to observe the DFKE in GaAs. We use ultrashort femtosecond pulses in a non-degenerate, non-collinear pump-probe configuration to measure the change in room temperature transmission of the probe pulse due to the DFKE. The pump pulse in our experiment comes from an Optical Parametric Amplifier (OPA), which is a tunable source of midinfrared (MIR) radiation, while the probe is a broadband white light continuum generated using a Chirped Pulse Amplifier (CPA). The probe transmission is recorded using a spectrometer having a multichannel CCD camera. In the following sections we describe in detail the various experimental techniques, instruments and the apparatus we used in our setup.

4.1 Lasers

The lasers used in our experiment are ultrafast femtosecond lasers. The extremely short pulse duration allows one to study the ultrafast dynamics of a system. Such lasers can also be used to produce laser pulses with enormous peak powers and power densities. In our experiments, we use this property of pulsed lasers to study extreme non-linear processes in semiconductors.

4.1.1 Chirped Pulse Amplifier (CPA)

Ultrashort pulses are generated by mode-locked lasers. By constructive interference, a short pulse is formed when many longitudinal modes are held in phase in a laser

resonator. Various techniques have been employed, usually grouped under *active* and *passive* mode-locking [23]. Modern solid-state mode-locked lasers use a different scheme called self-mode-locking and Ti:sapphire has become by far the most common laser material for the generation of ultrashort pulses. Ti:Sapphire has a gain bandwidth from 700 to 1100 nm peaking around 800 nm, the broadest of the solid-state materials yet discovered, and extremely good thermal conductivity. Self-focussing, based on the optical Kerr effect, is the basis of the Kerr lens mode locking (KLM) effect used in ultrashort lasers. The regenerative cavity of the laser usually consists of a Brewster-angle cut Ti:Sapphire rod doped to absorb about 90% of the incident pump radiation, two concave mirrors placed around it, a high reflector and an output coupler. A pair of Brewster-cut fused-silica prisms are inserted to control the spectral dispersion (chirp) introduced in the laser rod. Displacement of one of the curved mirrors by only 0.5 mm pushes the cavity into pulsed mode. The laser repetition rate can be adjusted by the insertion of a cavity dumper in the second fold, without affecting the pulse width. Alternatively, as in our case, a passively mode-locked Er-doped fiber laser is used as a source of pulses. After frequency-doubling the fiber output through a Nd:YAG laser, the output is fed to the Ti:Sapphire rod in the cavity. The amplification of nanojoule-level femtosecond pulses to the millijoule-level is complicated by the extremely high peak powers involved. The problem is cleverly overcome in a CPA by stretching the pulse in time using dispersion to advantage. This is followed by amplification and subsequent recompression to the original pulse duration. This technique also has the benefit of eliminating unwanted nonlinear effects in the amplifier materials. A diagram showing the principle of chirped-pulse amplification is shown in Fig. 4.1 [23].

In our experiments, CPA - 2010 (Clark MXR, Inc.) was used for probe pulse generation and also for pumping the OPA. Fig. 4.2 shows the basic configuration of
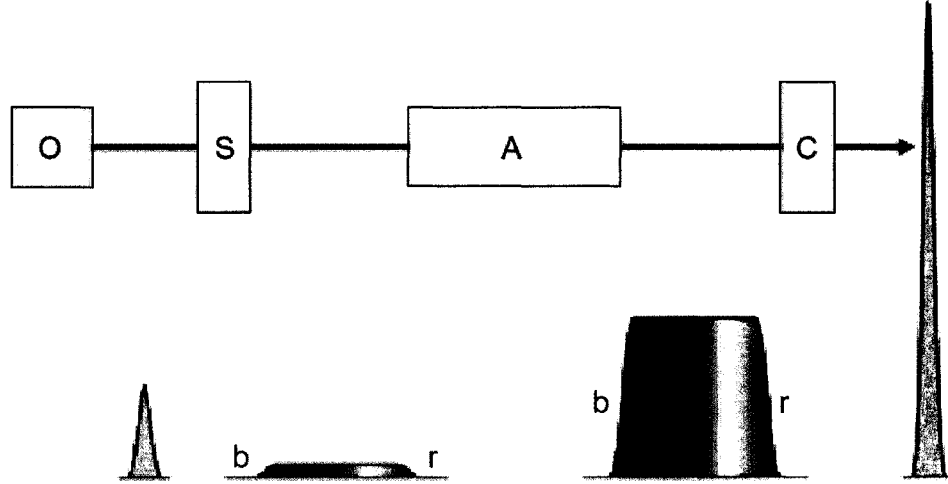
Figure 4.1 : The oscillator output is stretched in grating stretcher (S) such that the red frequency components (r) travel ahead of the blue (b). The peak intensity is reduced in the process. The stretched pulse is then amplified in a regenerative amplifier (A) before recompression in a grating-pair compressor (C). [23]

the system. A diode laser (980 nm) pumps a SErF femtosecond fiber oscillator, which provides femtosecond pulses with repetition rate in the 25 to 40 MHz range. These femtosecond pulses frequency-doubled by a Nd:YAG go through a pulse stretcher and seed a Ti:Sapphire regenerative cavity. A built-in fast photodiode inside the fiber oscillator cavity provides an input signal to a Pockels cell driver, which then generates reference signal to synchronize the timing of seed pulses, pump laser and cavity dumping. Finally, a pulse compressor compresses the amplified pulses to a duration of about 150 fs. The output of our CPA unit is about 1 W for 150 fs pulses at 780 nm with 1 kHz repetition rate.

Sketch of Clark CPA-2001+

Frequency-doubled
Nd:YAG laser

Diode laser

Femtosecond
SErF Fiber
Oscillator

Fiber
ring laser

Fast
photodiode

Pulse
stretcher

Ti:sapphire

Polarizer

Delay 2

Reference
driver

Regenerative
and Post
-amplifiers

Pockels
cell

Delay 1

Pockels
cell driver

in   out

Pulse
compressor

775 nm
1 kHz
1.3 mJ
150 fs
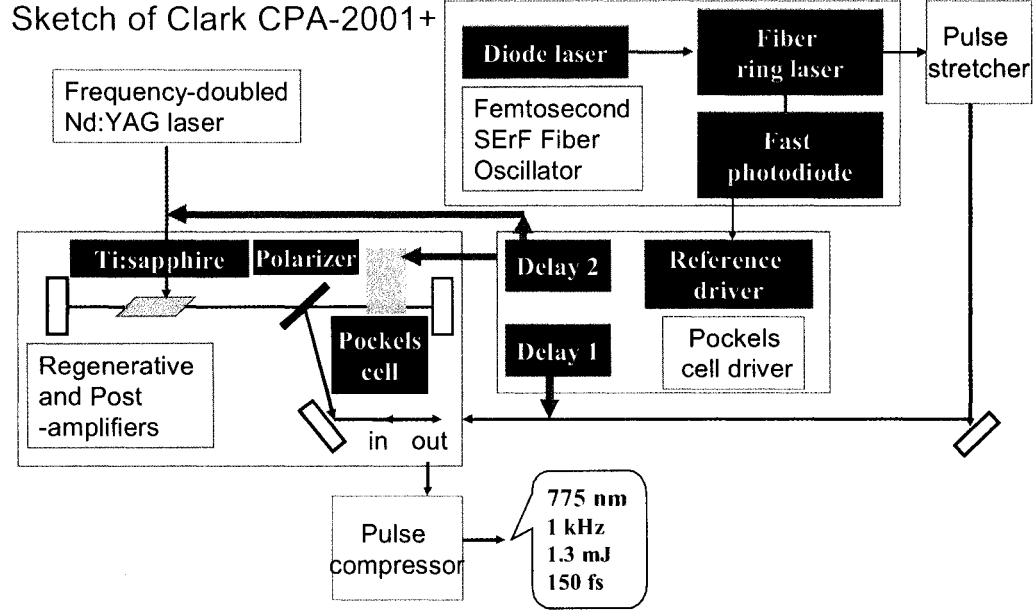
Figure 4.2 : Schematic sketch of the Clark CPA system.

4.1.2   Optical Parametric Amplifier (OPA)

As mentioned earlier, the pump pulses in our experiment are MIR pulses generated in an OPA which is pumped by the CPA. Most techniques in use now are based on parametric difference-generation (DFG) as shown in Fig. 4.3. In DFG, a strong femtosecond pulse at frequency $\omega_1 + \omega_2$ mixes in a nonlinear crystal with a weaker pulse at frequency ω_1, to produce a new beam of femtosecond pulses at frequency ω_2. If the incident power at frequency ω_1 and ω_2 is zero, a nonlinear cystal can produce them spontaneously from vacuum modes in a process referred to as optical parametric generation (OPG). If the incident power at frequencies is small but nonzero, the pump pulse at frequency $\omega_1 + \omega_2$ can amplify the former frequencies in what is referred to as OPA. Since the peak power of a femtosecond pulse can be extremely high while

the pulse energy is relatively low, one can produce enormous parametric gain without destroying the nonlinear crystal. The wavelengths that are produced in OPA depend on the phase-matching condition, group velocity walk-off and the type of crystal used. Beta-Barium Borate (BBO) is very efficient owing to the small group velocity walk-off and high damage threshold. KTP and its analogs rubidium titanyl phosphate and cesium titanyl phosphate are not as efficient but allow generation of femtosecond pulses at wavelengths as long as 3-4 μm. There is a variety of crystals suitable for generation of pulses in the MIR region such as $AgGaS_2$ and $GaSe$. However, when these crystals are used to convert directly from the visible to the MIR, they suffer from enormous group velocity walk-off, absorption of the pump and very poor efficiency. Therefore, generating MIR pulses is typically performed in a two-stage process: an OPA generates two NIR frequencies (e.g., 800 nm $\rightarrow$ 1.5μm + 1.7μm, in BBO) followed by a difference frequency mixing stage (e.g., 1.5 - 1.7 μm $\rightarrow$ 12μm, in $AgGaS_2$). Our OPA (Quantronix/Light Conversion's TOPAS) can provide tunable light from 522 nm to 20 μm. It uses a multipass to generate the final output pulses. When the pump is focussed onto the BBO crystal, it generates superflourescence, of which a small part is selected by a grating and then amplified in further passes through the crystal. For our experiments, this computer controlled OPA was used to provide MIR pulses from 4.7 μm to 14 μm, which served as our pump beam. Fig. 4.4 shows a schematic of a typical OPA [23].

4.1.3 Probe beam: White light continuum

At high intensities such as on the peak of an ultrashort laser pulse, the refractive index of any medium becomes a function of the incident intensity. This effect, which we discussed in Chapter 2, is called the optical Kerr effect (OKE) and can be described
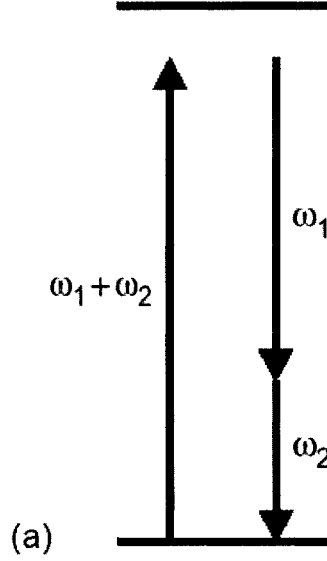
Figure 4.3 : Difference frequency mixing.

as

$$n(I) = n_0 + n_2 I + \cdots \qquad (4.1)$$

where n_0 is the normal refractive index of the medium and n_2 is the nonlinear refractive index. A laser pulse with center frequency ω traveling through a medium of length L will acquire an optical phase $\omega L n / c$ and therefore the effects of the nonlinear refractive index will become important when this phase factor becomes comparable to a wavelength. The OKE can modify the spectral properties of an ultrashort pulse. The electric field of a laser pulse traveling in the x direction can be written as

$$E(t) \cos(\omega t - kx) \qquad (4.2)$$

where $k = \omega n / c$ is the wavenumber. Since the wavenumber depends on the nonlinear refractive index of the medium, the pulse will acquire a time-dependent phase. After
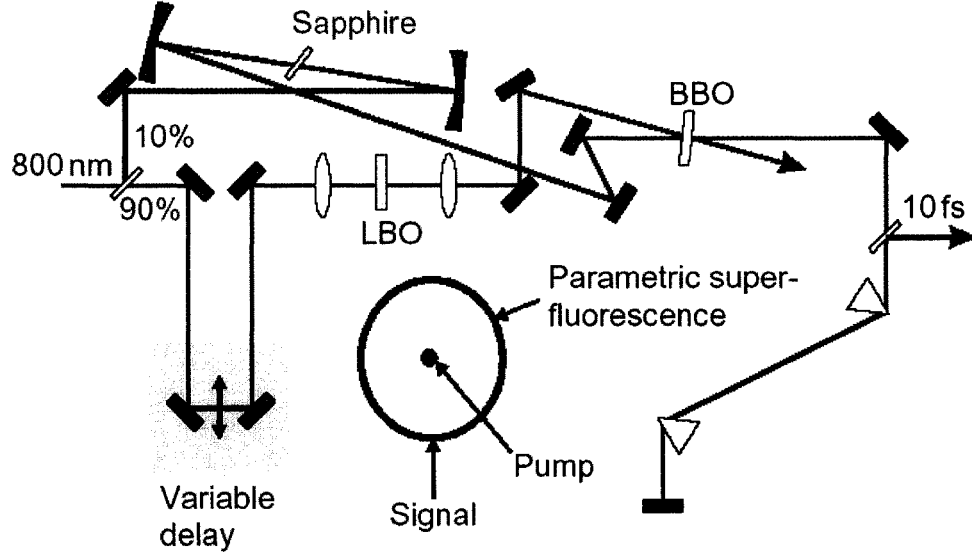
Figure 4.4 : Schematic of an OPA [23].

such a modification, one finds

$$E(t) \cos((\omega + \xi t)t - kx) \tag{4.3}$$

where ξ depends on the nonlinear refractive index, the pulse width, the peak power, and the distance traveled. Thus, the nonlinear refractive index induces a chirp on the pulse. In other words, the spectrum of the pulse has broadened owing to the nonlinear interaction. This is called self-phase modulation. In our experiment, we make use of this effect to generate white light continuum (400 nm to 1.6 μm) by focussing about 10% of CPA beam on a sapphire crystal. This white light continuum acts as our probe beam.

4.2 Detectors

We recorded the transmission of the probe beam using a spectrometer with a CCD camera attached to it. Also for obtaining temporal overlap between the pulses we had to monitor the pump beam signal using a HgCdTe detector.

4.2.1 Spectrometer

To measure the transmission spectra of the probe beam we used an Acton Research SpectraPro 300i with a liquid nitrogen cooled CCD array attachment. The spectrometer has triple-grating turret which can be remotely controlled using a computer. It has a scan range of 0 - 1400 nm with a resolution of 0.1 nm at 435.8 nm.

4.2.2 MCT detector

For obtaining the temporal overlap of the two pulses we needed to monitor the MIR pump signal. As the HgCdTe (MCT) is sensitive in the MIR range, we used Electro-Optical Systems Inc.'s low temp MCT detector. Its spectral range is 2 - 20 μm with a peak in responsivity at 18 μm.

4.3 Experimental Setup

The experimental setup for observing the DFKE is shown in Fig. 4.5. The CPA beam is split using a 90:10 beam-splitter. The larger fraction of the power is fed to the OPA to generate MIR pump pulses while the small fraction is used for white light generation. The two pulses are then focussed onto the sample using a parabolic mirror. The spatial overlap of the pulses is achieved by passing both beams through a 50 μm pinhole at the focus. This is roughly the spot size of the pump beam which cannot be further decreased owing to the longer wavelength of the pump. The probe

on the other hand is focussed to a much smaller size using the same parabolic mirror, as is required in any pump-probe experiment. A computer-controlled delay stage (Newport ESP 300 Motion Controller) is used to temporally overlap the two pulses. We monitor the transmission of the MIR beam through the GaAs sample using a liquid nitrogen cooled MCT detector. The MIR pump beam is far less energetic ($\sim$ 100 meV) compared to the band gap of GaAs (1.4 eV) and hence no carriers are created by it. On the other hand, white light pulse has components which are more energetic than the band gap of GaAs and hence can create real carriers. The MIR radiation can cause excitations of these real carriers causing its own transmission to decrease. The creation of carriers also affects the refractive index of the sample. This way by varying the delay stage we can achieve the temporal overlap looking at the change in transmission of the MIR beam induced by the generated charge carriers. Once this is achieved, we record the transmission spectra of the probe beam which is sent to the spectrometer.

4.4 Samples studied

For our experiments we used two samples of GaAs. The first sample, about 350μm thick semi-insulating GaAs wafer, was used to study the below band gap absorption. The second sample which was a few microns thick was used to study the above bandgap features. It was prepared by taking a GaAs substrate which was coarsely polished down to about 100 microns. On top of the substrate, a thin etch-stop AlGaAs layer (with high Al content) followed by the GaAs film was grown by MBE. Using a transparent low temperature epoxy, the epitaxial side was affixed to a glass slide, avoiding any trapped air bubbles. The remaining part of the GaAs substrate was etched using a slow etchant which was a mixture of citric acid and hydrogen peroxide. This etchant stops on the AlGaAs layer which can then be removed using
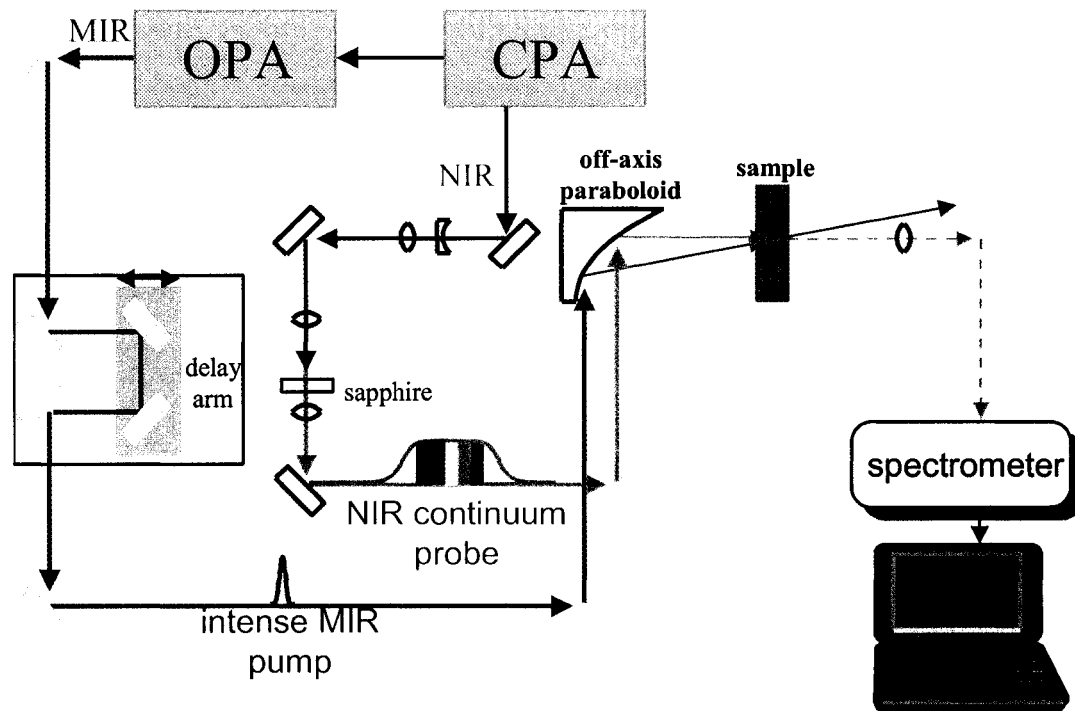
Figure 4.5 : Schematic diagram of the experimental setup to observe the DFKE.

hydrochloric acid and water, leaving the required GaAs film sample on the glass slide.

Chapter 5

Experimental Results and Discussions

In this chapter we present results of our experiments done on GaAs samples at room temperature. We investigated both below and above band gap changes induced by the strong MIR pump.

5.1 Below band gap absorption

First we tried to observe the below band gap absorption predicted by the theory. For this we used a bulk GaAs wafer about 350 μm thick as our sample. The pump beam contained some residual signal and idler from the OPA and had to be filtered using proper long wavelength pass filters. Also the white light contained strong signal at 780 nm from the CPA which was filtered using appropriate longpass filters. After putting the filters in the beam path, which introduced delay in both beams, the timing zero had to be found again by varying the motorized delay stage. Fig. 5.1 shows a plot of normalized transmission of the probe beam in the presence of the pump beam below the band edge as a function of photon energy. As can be seen from the graph, there was huge absorption of probe beam below the band edge (1.42 eV) which led to *almost complete quenching of the transmission*. We measured the transmission for different pump wavelengths and found that the quenching was more pronounced for higher wavelengths *in spite of the fact that the OPA output intensity decreases for higher wavelengths*. This counterintuitive observation can be explained from the fact that the ponderomotive potential increases for higher wavelengths due the λ^2
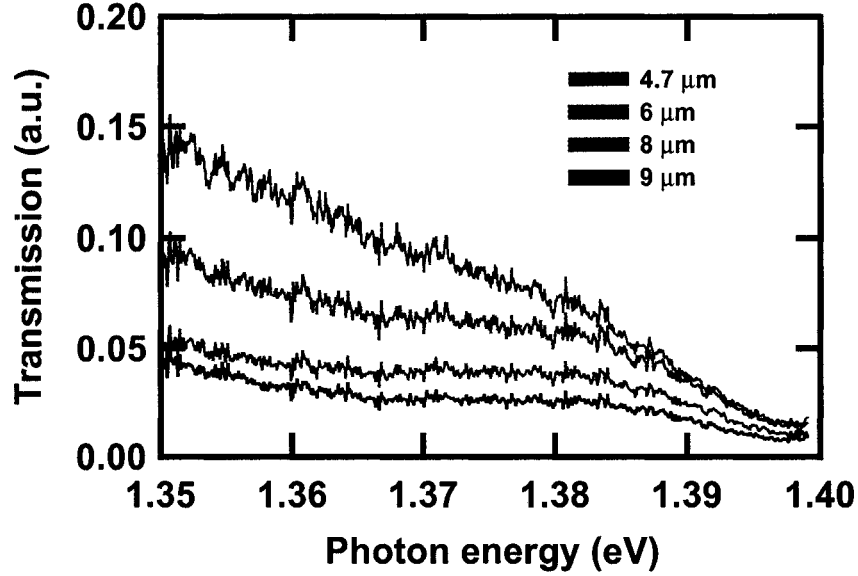
Figure 5.1 : Transmission quenching below the band gap in the presence of a strong MIR pump beam of different wavelengths. The effect increases with increasing wavelength despite the fact that intensity of our MIR source decreases for longer wavelengths. This is because, for our case, the ponderomotive potential is larger for longer wavelengths.

dependence and hence we see a much more pronounced effect at higher wavelengths. This peculiar wavelength, power dependence differentiates the DFKE from any known nonlinear optical process in solids. We do not have a precise measure of the power of the pump but we estimate the peak intensity at the focus to be around 10^9 - 10^{10} W/cm^2 for a pump wavelength of 9 μm. From this value we obtain the ratio of U_p and $\hbar\omega$ to be about 0.5 for 9 μm.

Next we studied the dependence of this effect on the time delay between the pump and the probe beams as shown in Fig. 5.2. The effect was observed *only* when the two pulses overlapped temporally confirming the effect to be a virtual one. The observed asymmetry about timing zero is because of significant chirp in the white

light probe. It should be mentioned here that previous observation of below band gap absorption by Chin *et al.* [17] using picosecond pulses was not as drastic as our observation using femtosecond pulses, which is an almost complete quenching of the probe transmission. This quenching of absorption below the band gap and its unusual wavelength and power dependence agrees well with the predicted theory. The probe power was varied using neutral density filters but the effect showed no dependence on the probe power, thereby excluding the possibility of any multiphoton absorption of the probe beam. The unusual power and wavelength dependence which we observed, rules out the possibility of multiphoton absorption involving both pump and the probe photons. If there is any multiphoton interband absorption of the pump photons, there would be generation of real carriers whose effect would remain even after the pump and the probe pulses do not overlap. However, we do not see any such long-lived effect. Also according to Keldysh [24], the probability of multiphoton pump absorption is high only when $\gamma \gg 1$ where,

$$\gamma = \omega \left(mE_g \right)^{1/2} / eE. \tag{5.1}$$

In our case however, we estimate γ to be about 1.8 and hence we are far away from the multiphoton regime. It should be noted here that the below bandgap absorption we observe is due to the photon-assisted (photon of the probe beam) tunneling of electrons to the conduction band, which is very different from the (Zener type) direct tunneling of electrons across the bandgap due to the electric field of the pump beam. In order to observe such a direct tunneling, very high intensity of the pump beam would be required.
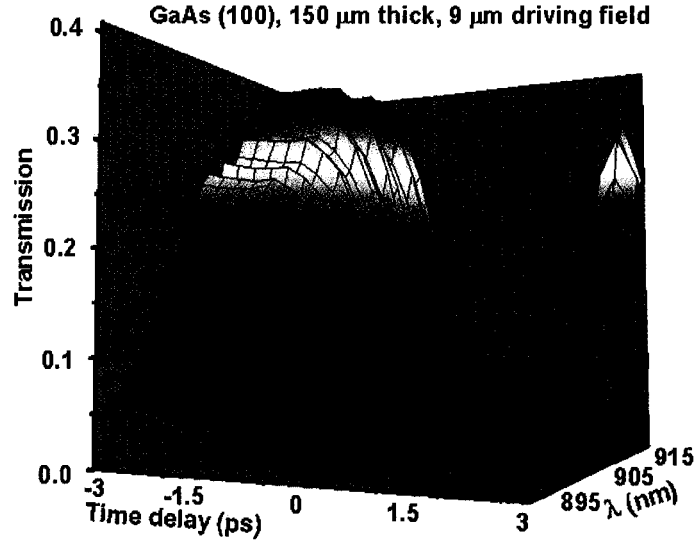
Figure 5.2 : Time dependence study of the transmission below the band gap in presence of a pump beam of 9 μm wavelength.

5.2 Franz-Keldysh oscillations

In order to observe oscillatory behavior in the transmission spectra above the band gap, we used a GaAs film sample which was a few microns thick. This reduced the absorption above the band edge making it possible to measure the above band gap transmission. Fig. 5.3 shows the transmission of probe through the film sample in the presence of 9 μm MIR pump. As can be seen from the figure, we were indeed able to see oscillatory behavior above the band gap when the pump and probe pulses overlapped temporally. However, the transmission spectra taken away from the temporal overlap of the pump and the probe beams do not show these oscillations, demonstrating the ultrafast nature of the process. This to our knowledge is the first experimental observation of above band gap oscillation due to the DFKE. A large, almost 40 % induced transparency was also observed just above the band gap as a feature of these
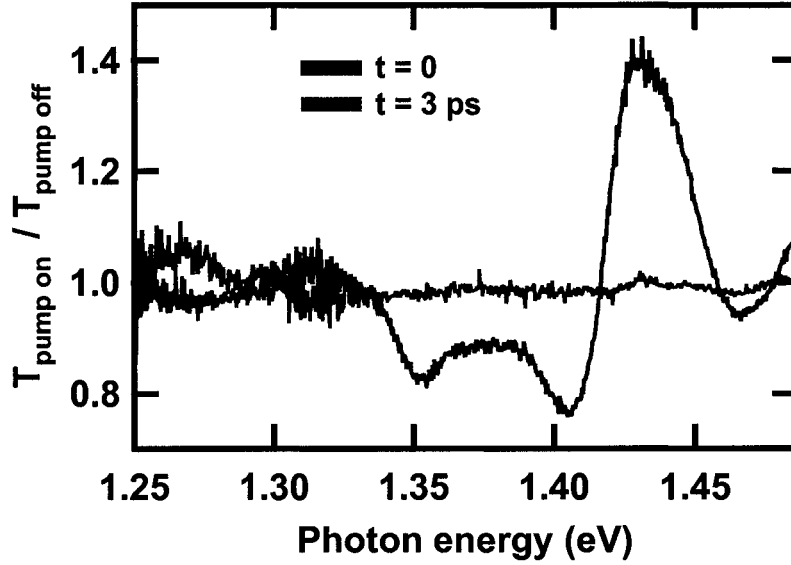
Figure 5.3 : Transmission spectra of the probe beam through GaAs film sample for different time delays between the pump (9 μm) and the probe beams. Oscillations are observed above the bandgap (1.42 eV) only when the two beams overlap temporally. Note the pronounced ($\sim$ 40%) induced transparency right above the bandgap.

oscillations. This corresponds to a change in absorption coefficient of about 17 %. The observed photoinduced transparency represents a novel phenomenon quite unlike the well known self-induced or electromagnetically induced transparency [25] and can be explained only on the basis of DFKE.

In Fig. 5.4, intensity dependence for fixed wavelength of pump (9 μm) is shown. As expected, the oscillations became weaker for lower intensities of the pump beam. Finally, the dependence of the effect on the pump wavelength was studied. Fig. 5.5 shows a plot of probe transmission for different wavelengths. As can been seen from the figure, oscillations can be better resolved at longer wavelengths. This trend is similar to the below bandgap case and can be explained on the basis of ponderomotive potential. We did not observe a significant change in the period of oscillations for
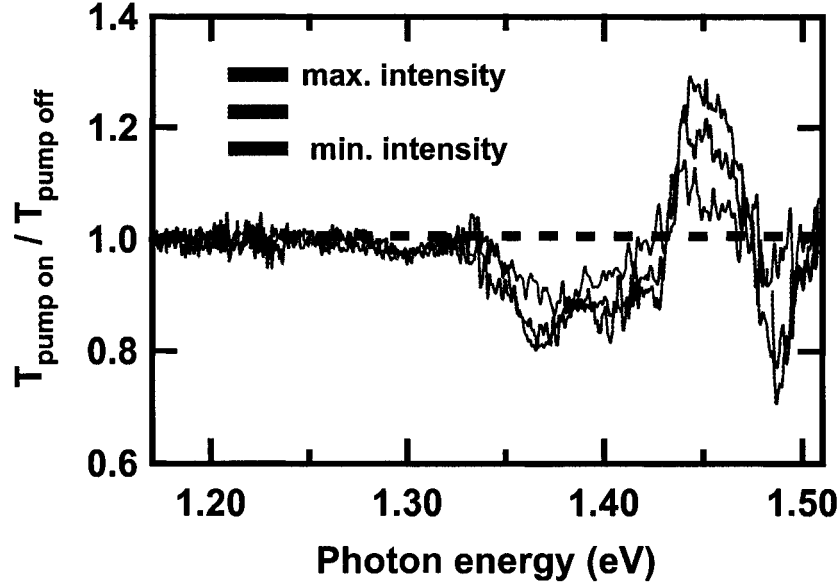
Figure 5.4 : The observed change in transmission spectra of the probe beam in presence of the pump beam (9 μm) for different intensities.

different wavelengths as we expect the ratio of ponderomotive potential U_p to the photon energy $\hbar\omega$ to be similar in magnitude (about 0.5) for all the cases. However, careful observation of Fig. 5.4 and Fig. 5.5, shows slight shift of the peaks when intensity and wavelength of the pump beam are varied. It should be mentioned here that the intensity of the pump at 7 μm was higher compared to the intensity at 9 μm (7 μm is just away from the strong water absorption peak close to 6 μm).

5.3 Experimental fit

Theoretical calculations done by Y. Yacoby predict an exponential tail in the absorption spectra below the band gap and oscillatory behavior above the band gap [1]. He starts with a time-dependent wavefunction (modified Houston wave function) which is solution to the time-dependent Schrödinger equation with the electromagnetic field
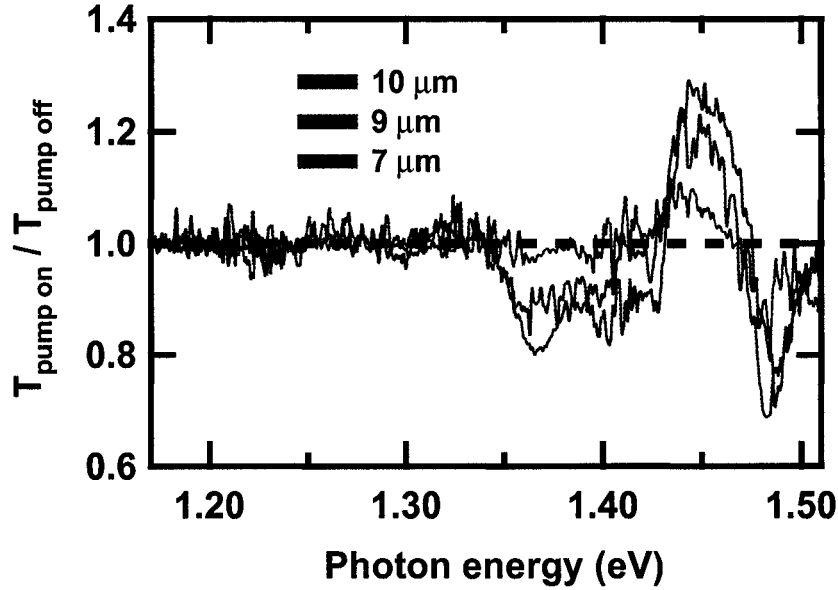
Figure 5.5 : Transmission spectra of the probe beam for different pump wavelengths. The intensity of the pump beam decreases with increasing wavelength. The observed effect is more pronounced at longer wavelengths, even though the intensity of the pump beam decreases with increasing wavelength.

of frequency ω (pump beam) included in the Hamiltonian. The transition rate between two such states due to an additional perturbation of frequency Ω (probe beam) is then found. In our experiments, we measured the time-averaged transmission of the probe beam and hence we calculated the time-averaged change in the transition rate from Yacoby's theory (see Eq. (38) in [1]). For comparison with the theory, the abscissa of Fig. 5.3 was changed from $\hbar\Omega$ (photon energy) to $\hbar\Omega - E_g$, where E_g is the bandgap of GaAs, and expressed in units of $\hbar\omega$. The values of intensity, wavelength and the effective mass for the calculation were taken to be $I=10^9$ W/cm^2, $\lambda=9$ μm, and $m^*=0.067$ m.

Fig. 5.6 shows plots of theoretically calculated and experimentally observed change in the absorption against the normalized photon energy. The ordinate of
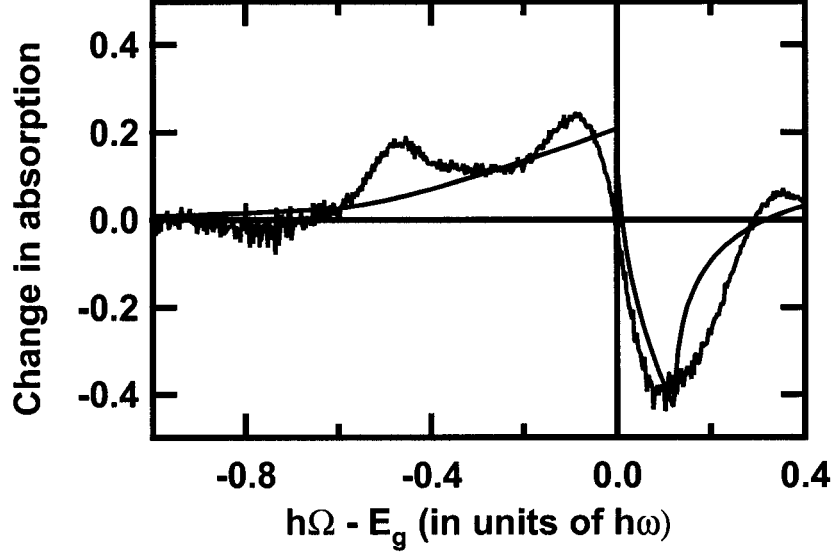
Figure 5.6 : Plots of the calculated and the experimentally observed changes in the absorption as a function of normalized photon energy of the probe beam. The calculated curve captures the essential features of our observation reasonably well.

the calculated curve was scaled for comparison with the observed curve. As can be seen from Fig 5.6, our experimental data agrees well with the theoretical prediction. The agreement with the theory is remarkably good above the bandgap, given the fact that we have *not* used any fitting parameters in our calculations. Yacoby's theory inspite of being oversimplistic, explains our experimental observations above the band gap extremely well. Below the bandgap, however, the theory predicts a monotonous decrease in the absorption, whereas our data show some additional peaks over the decaying absorption. We do not have any satisfactory explaination for this observation and further theoretical and experimental studies are needed in order to completely understand this unexpected discovery.

Chapter 6

Applications to All-Optical Switching

The growth of telecommunication networks has led to an unprecedented demand for larger and larger bandwidths. The upgrade from electronics to photonics to deal with this demand has resulted in optical networks which offer Gbps data speed. To further increase the bandwidth of existing optical networks, wavelength division multiplexing (WDM), wherein multiple wavelengths of light are used to send data simultaneously over a single fiber, has been proposed. An essential requirement of WDM is switching data at one wavelength to another wavelength. Such switching can be done using optoelectronic techniques in which the optical signal is converted to electrical signal and switching takes place in the electrical domain. All-optical wavelength conversion, on the other hand, avoids this roundabout procedure by switching directly in the optical domain as shown in Fig. 6.1. Thus all-optical switching is much faster than optoelectronic switching and is a promising option which needs to be considered for the future of high speed broadband networks. In this chapter we explore the idea of exploiting the DFKE for all-optical switching.

We first look at the requirements of WDM before reviewing various available wavelength conversion techniques. Finally, we propose two schemes based on the DFKE which look promising for all-optical switching.
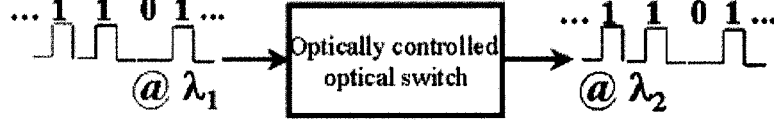
Figure 6.1 : A cartoon showing the scheme of all-optical switching

6.1 WDM

In present day telecommunication networks, optical techniques, in which carrier wave belongs to the optical domain, are widely used. The wave modulation allows transmission of digital signals up to a few gigabits per second on a carrier of very high frequency. The bit rate can be increased further, using several carrier waves that are propagating without significant interaction on the same fiber. This technique is called WDM [26]. With WDM, it is possible to couple sources emitting at different wavelengths λ_1, λ_2, ... λ_n into the same optical fiber. After transmission on the fiber, the λ_1, λ_2, ... λ_n signals can be separated towards different detectors at the fiber extremity (Fig. 6.2 [26]). Acceptable 160-channel grating-WDM components are already being manufactured. The main problem in increasing the number channels is acquiring enough stable fixed or tunable sources.

6.2 Wavelength conversion techniques

Different techniques have been proposed to perform wavelength conversion. In this section we concentrate on the following:

1. Cross-modulation techniques including cross-gain modulation (XGM), and cross phase modulation (XPM)

$$\lambda_1 + \lambda_2 + \lambda_3 + \lambda_i + \lambda_j$$
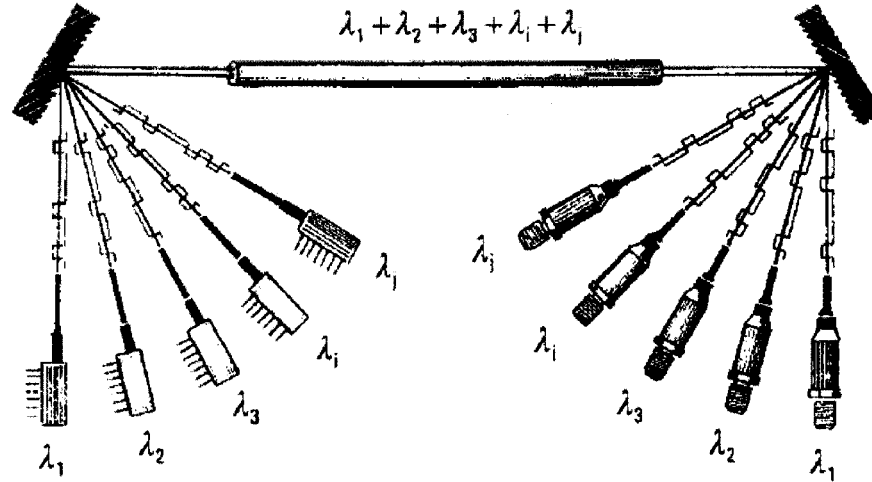
Figure 6.2 : Illustration of WDM [26].

2. Coherent techniques including four-wave mixing (FWM) and difference frequency generation (DFG)

6.2.1 XGM

This wavelength conversion principle is based on nonlinearities in semiconductor optical amplifiers (SOAs). Before discussing XGM, we briefly discuss the principle of a semiconductor optical amplifier.

SOA

An SOA is based on the same technology as a Fabry-Perot diode laser. Such a laser consists of an amplifying medium located inside a resonant (Fabry-Perot type) cavity. In order to get only amplification function, it is necessary to avoid self-oscillations generating the laser effect. This is accomplished by blocking cavity re-

flections using antireflection coating. Unlike erbium-doped fiber amplifiers, which are optically pumped, SOAs are electrically pumped by injected current. SOAs in the InP/InGaAsP material system are of most interest because they produce gain in the wavelength bands of modern fiber systems (i.e., 1530-1565 nm). A schematic diagram of an SOA device is shown in Fig. 6.3 [27]. It consists of a forward biased p-n heterojunction through which current flows, and optical waveguides to confine the incoming lights to the active region. Anti-reflection coatings are applied to the input and output facets of the device to prevent optical feedback. A large carrier concentration buildup within the active layer results in a population inversion and optical gain via stimulated emission for an injected signal. The rate of stimulated emission in an SOA is dependent on the optical input power. At high optical injection, the carrier concentration in the active region is depleted through stimulated emission to such an extent that the gain of the SOA is reduced. This effect is known as gain saturation. Gain saturation can be used to convert data from one wavelength to another as depicted in Fig. 6.4 [27]. Two optical signals enter a single SOA with one carrying amplitude modulated data and the other being a CW laser. If the peak optical power in the modulated signal is near the saturation power of the SOA, the gain will be modulated in synchronism with the power excursions. When the data signal is at a high level, the gain is depleted, and vice versa. This gain modulation is imposed on the unmodulated input beam. Thus, an inverted replica of input data is created at the target wavelength. The use of long SOA under high optical injection has enabled wavelength conversion up to 80 Gbps. The attractions of XGM wavelength conversion devices lie in their simplicity, high conversion efficiency, polarization independence, and insensitivity to the wavelength of the input data (provided it is within the SOA gain bandwidth). The main disadvantage of devices using XGM for wavelength conversion is the degradation of extinction ratio. This can be a seri-
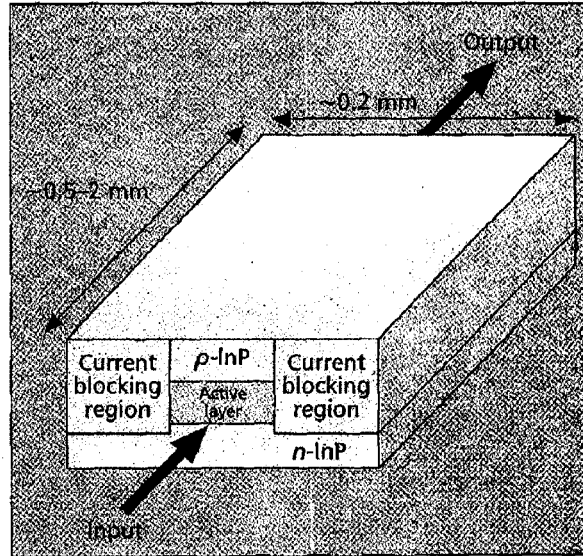
Figure 6.3 : A typical SOA [27].

ous limit to cascadability of such devices in an optical network. Another important drawback of XGM is the chirp induced on the target waveform due to simultaneous modulation of the refractive index of the SOA.

6.2.2 XPM and Interferometric devices

Non-linearities in an SOA can also cause modulation of refractive index. This cross phase modulation (XPM) can be utilized in interferometric arrangements with significant advantages over those relying XGM alone. In such devices the light to be switched is split into two paths containing SOAs, and a relative phase shift is induced by the optical switching signal entering one of the SOAs, which saturates the gain. When light is recombined, constructive or destructive interference will occur depending on the phase difference between the two paths. Fig. 6.5 [27] shows examples of
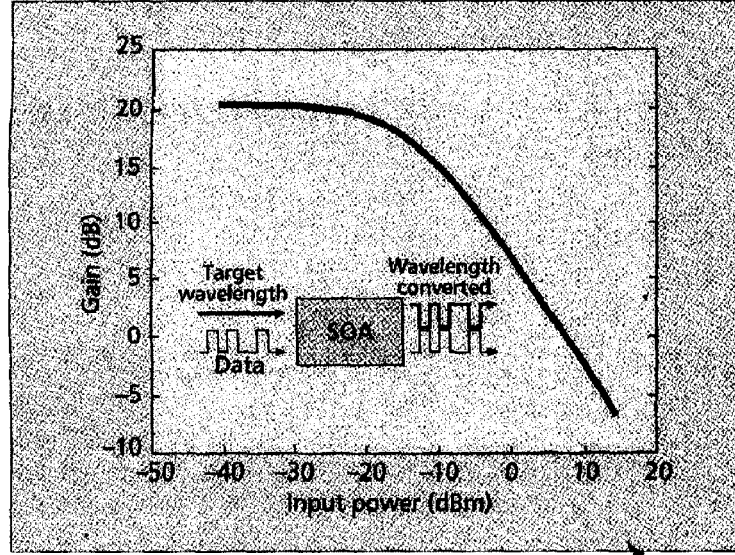
Figure 6.4 : SOA gain saturation characteristic and operating principle of a XGM wavelength converter [27].

interferometric devices based on Michelson and Mach-Zehnder interferometers. XPM schemes show improvement on extinction ratio, increasing their cascadability, and low chirp than XGM. However, precise control of phase is required for their efficient working.

6.2.3 FWM

Another promising approach to wavelength conversion is to utilize four-wave mixing (FWM). In FWM, the input signal at frequency ω_i is added to a CW pump at frequency ω_p in a nonlinear optical medium. A signal at frequency $\omega_c = 2\omega_p - \omega_i$ is generated (Fig. 6.6 [26]). The conversion efficiency can be very high in an SOA with a long cavity. As FWM is a coherent process, the wavelength conversion is independent of modulation format. Also it is not restricted by intrinsic carrier lifetime like XGM
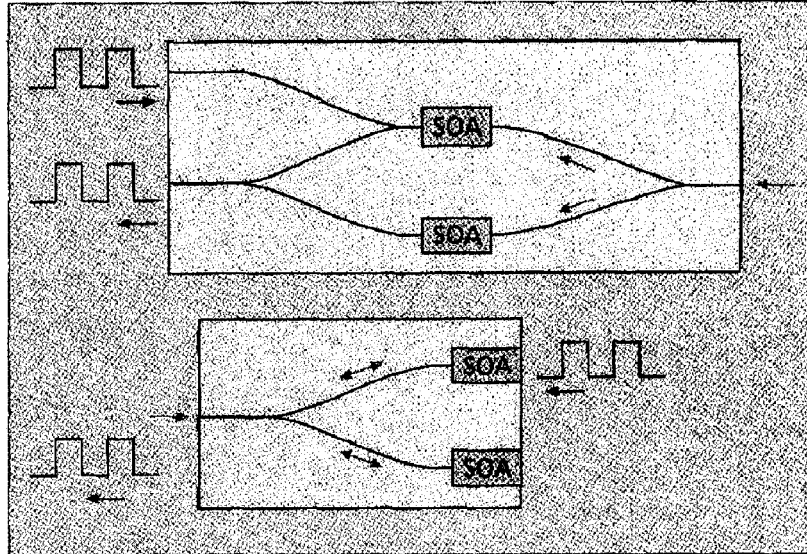
Figure 6.5 : Wavelength conversion using Mach-Zehnder and Michelson interferometric configuration [27].

and XPM. The inherent polarization sensitivity can be avoided by using two pumps or other compensations. FWM wavelength converters have been demonstrated to work at 40 Gbps.

6.2.4 DFG

In DFG, second order non-linearity of an optical medium is used to generate an output beam at the difference frequency of pump and input. DFG allows for multichannel wavelength conversion and is largely insensitive to the polarization of the input beam. Being a coherent process, it is ultrafast. However, its efficiency and the pump tunability need to be improved. Other schemes utilizing the QCSE [28] and intersubband absorption [29] have also been proposed but they are both limited by carrier lifetime as carriers play the crucial role in switching. Also they are not
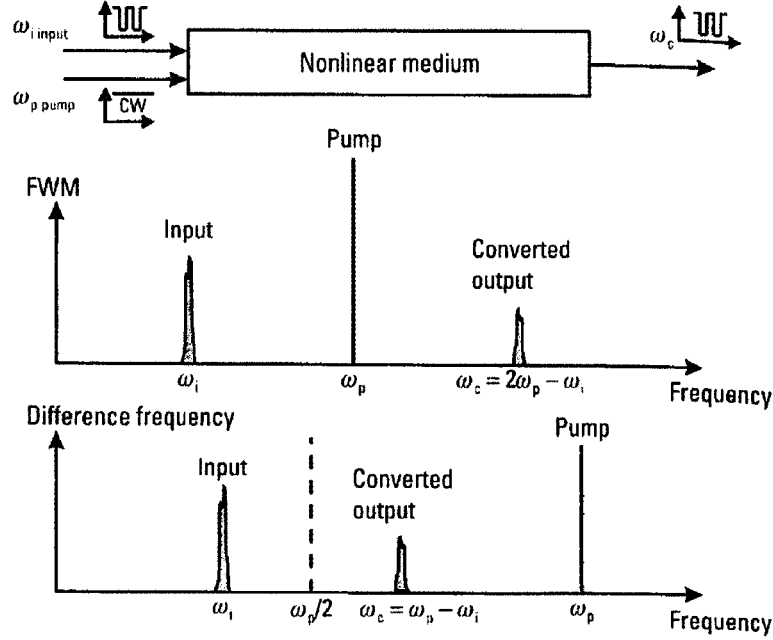
Figure 6.6 : Wavelength conversion using FWM [26].

polarization insensitive.

6.3 Our schemes

In this section we propose two schemes which utilize the DFKE for all-optical wavelength conversion. Both schemes are ultrafast and physically realizable. The first scheme uses carriers for switching but is very simple in design, whereas the second scheme is fully coherent in nature.

6.3.1 Scheme I

In both schemes we use a MIR pump beam to induce below bandgap absorption and hence cause modulation of the input beams with photon energies smaller than

the band gap. This scheme allows for ultrafast simultaneous conversion to multiple wavelengths and is completely polarization insensitive. Depending on the wavelengths to be switched, a material can be suitably chosen whose band edge corresponds to a photon energy which is larger than the photon energy of the shortest wavelength. For example, if the shortest wavelength to be switched is 890 nm, GaAs with a band gap of 1.42 eV can be used. The only requirement is that the MIR pump energy should be much smaller than the band gap. From our experimental data for GaAs we see that the range of wavelengths which get affected by the DFKE is more than 70 nm, which is sufficiently broad to allow for WDM. In our experiments we used intense MIR to completely quench the transmission below the band gap but for all-optical switching, we could do with a lot less power. Such intensities can be obtained from MIR quantum cascade lasers operating in pulsed mode, thus avoiding the need of an OPA.

The next step is to switch the input data of an arbitrary wavelength to MIR pump. This can be done using a material whose band gap is slightly smaller than the photon energy of the input beam (ideally we choose a material whose band gap is smaller than the photon energy of the longest wavelength input). This way the input creates real carriers and causes absorption of the MIR pump. Thus we transfer inverted data to the MIR pump which is again inverted and transferred to the final output wavelength. Hence we get back to the same data after two inversions. As we are using real carriers for transferring the data to the MIR pump, the speed of switching is limited to the intrinsic carrier lifetime which is on the order of nanoseconds. This severely slows down the overall switching speed. To avoid this, we propose the use of low temperature grown semiconductors with extremely short carrier lifetimes of a few picoseconds [30]. Thus we can expect close to Tbps switching speeds. In low temperature grown semiconductors, many defects are created which act as traps
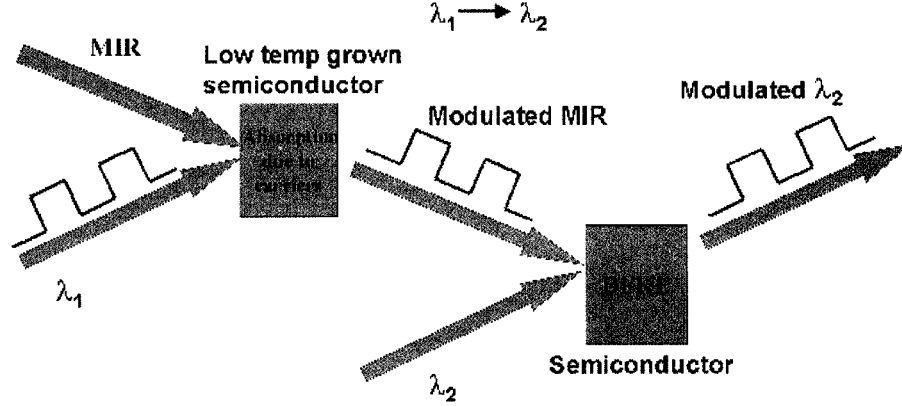
Figure 6.7 : Scheme I

to relax the carriers extremely fast. The exact mechanism of carrier relaxation in low temperature grown semiconductors is still not very clear. In spite of two step conversion ($\lambda_1 \rightarrow MIR \rightarrow \lambda_2$), our scheme is ultrafast and extremely simple to implement. Fig. 6.7 illustrates the principle of this scheme.

6.3.2 Scheme II

This scheme is similar to the first one expect for the switching of the MIR pump. Instead of using carriers for switching, we propose a fully coherent method for this scheme. To switch $\lambda_1 \rightarrow MIR$, we first use DFG to generate MIR radiation. This can be done in a suitably designed SOA. Thus the information from the signal beam gets transferred to the MIR beam. In the next step, we amplify the MIR beam using a quantum cascade MIR laser working as an SOA [31]. After this we have sufficient intensity in the MIR beam to cause the DFKE. This amplified MIR pump can then be used to switch many wavelengths, longer than the wavelength corresponding to the bandgap of a suitably chosen material, simultaneously using the DFKE. Fig. 6.8
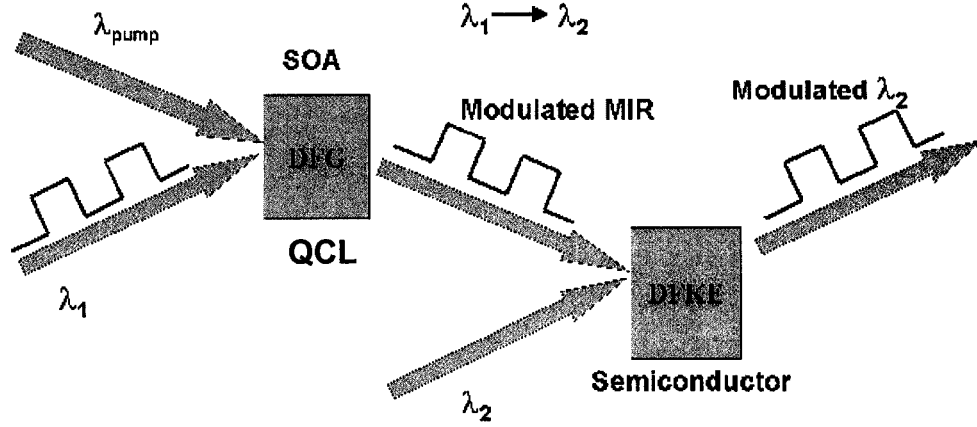
Figure 6.8 : Scheme II

illustrates the principle of this scheme. One advantage of this scheme over the DFG
wavelength conversion (Sec.6.2.4) is that no tunability of pump is required as we
switch all the wavelengths using an intermediate MIR pump. This is because the
second step which uses the DFKE for switching, is not very sensitive to the MIR
pump wavelength. Thus using an intermediate MIR pump, we remedy the problem
of pump tunability, inherent in the DFG wavelength conversion technique.

In conclusion, our schemes based on the DFKE are ultrafast, simple and easily
implementable. They offer possibilities for multichannel switching which are polar-
ization insensitive apart from having other advantages like low-output chirp.

Chapter 7

Conclusions and Future Work

In summary, we experimentally investigated the DFKE in GaAs. We were able to observe below bandgap absorption for MIR pump beam of different wavelengths. For the bulk case, we observed almost complete quenching of the transmission for photon energies more than 100 meV below the band edge. This is in agreement with the earlier report on below bandgap absorption due to the DFKE and also agrees well with the theoretical calculations. The existing theories predict observation of the DFKE when ponderomotive potential of the pump beam is comparable to its photon energy. Our experimental observations verify this fact and also agree qualitatively with the λ^2 dependence of the effect due to the ponderomotive potential, i.e., the effect is more pronounced for longer wavelengths despite the decrease in intensity. We also observed, for the first time, above bandgap oscillations in the film sample which is again in agreement with the theory. As a consequence of FK oscillations we observed a large photoinduced transparency just above the band edge. This is a completely novel phenomenon quite unlike other observations of transparency in solids and might have possible future applications. Our data does not show the blue shift of the band edge predicted by Johnsen *et al.*, though it agrees well with Yacoby's predictions. We do not expect to see any clear blue shift in $3d$ systems due to the smooth variation of the DOS. Such a shift might be more prominent in lower dimensional systems where the DOS shows sharp features near the band edge. The pump intensity and wavelength dependent data show trends which again agree

well with the ponderomotive potential picture. Our attempt to fit the data based on the calculation done by Yacoby is reasonably successful as it captures the essential features of the effect fairly well. One must note here that the fit is based on a very simplistic model but still manages to explain most of our observations accurately enough given the uncertainty in our estimation of the pump power. We were able to see some peaks below the bandgap which, are not predicted by Yacoby's theory.

As a possible application of this effect, all-optical wavelength converters required in modern day optical networks using WDM, were proposed. Our schemes, exploiting the below bandgap absorption due to the DFKE, meet most of the requirements of an ideal wavelength converter. They are ultrafast, polarization insensitive and easy to implement. Using quantum cascade lasers, one can think of a tabletop all-optical switch with Tbps switching speeds. In present day industry, DFG based converters are thought to be the most promising candidates for all-optical switching. Our scheme overcomes the problem of pump tunability which is inherent in DFG based switch by making use of a two step approach. However, this approach does not limit the speed of switching as the DFKE induced absorption is an ultrafast process. Thus our schemes based on the DFKE hold potential for industrial applications.

7.1 Future directions

It would be interesting from a scientific research point of view to study the DFKE in other systems including quantum confined structures such as quantum dots and carbon nanotubes. Such a study will shed new light on the optical properties of such system under intense laser field. It is important to verify if any blue shift of the fundamental absorption edge is indeed observed in lower dimensional systems. Also it needs to be verified whether any peaks below the bandgap are present in the absorption spectra as observed by us in the bulk case. There have been many

interesting theoretical predictions such as the collapse of band width [32] of solids under intense laser fields. Such predictions should be experimentally verified as an extension of the DFKE.

The DFKE offers ways to coherently control the band structure of a semiconductor. The changes in the optical properties near the band edge, brought about as a manifestation of the DFKE may find many applications. As a first step, the photoinduced transparency should be investigated in other systems for novel applications. From a more technological point of view, the schemes proposed in this thesis for all-optical switching need to be demonstrated and optimized for possible industrial applications. The work would involve designing the semiconductor amplifier and also careful material selection for the switch. The proposed scheme using quantum cascade semiconductor optical amplifiers looks promising and a detailed benchmarking and characterization of the device will actually test its feasibility for industrial applications.

Bibliography

[1] Y. Yacoby, "High-Frequency Franz-Keldysh Effect," Phys. Rev. **169**, 610 (1968).

[2] R. Boyd, *Nonlinear Optics* (Academic Press, San Diego, 1992).

[3] F. Agulló-López, J. Cabrera, and F. Agulló-Rueda, *Electrooptics: Phenomena, Materials and Applications* (Academic Press, San Diego, 1994).

[4] H. Haug and S. Koch, *Quantum Theory of the Optical and Electronic Properties of Semiconductors* (World Scientific, New Jersey, 1998).

[5] C. Hamaguchi, *Basic Semiconductor Physics* (Springer, New York, 2001).

[6] M. Cardona, *Modulation Spectroscopy* (Academic Press, New York, 1969).

[7] R. N. Bhattacharya, H. Shen, P. Paryanthal, F. H. Pollak, T. Coutts, and H. Aharoni, "Electroreflectance and photoreflectance study of the space-charge region in semiconductors: (In-Sn-O)/InP as a model systemlls," Phys. Rev. B **37**, 4044 (1988).

[8] D. A. B. Miller, D. S. Chemla, and S. Schmitt-Rink, "Relation betweeen electroabsorption in bulk semiconductors and in quantum wells: The quantum-confined Franz-Keldysh Effect," Phys. Rev. B **33**, 6976 (1986).

[9] S. Schmitt-Rink, D. S. Chemla, and D. A. B. Miller, "Linear and nonlinear optical properties of semiconductor quantum wells," Adv. in Phys. **38**, 89 (1989).

[10] D. A. B. Miller, D. S. Chemla, T. C. Damen, A. C. Gossard, W. Weigmann, T. H. Wood, and C. A. Burrus, "Band-Edge Electroabsorption in Quantum Well Structures: The Quantum-Confined Stark Effect," Phys. Rev. Lett. **53**, 2173 (1984).

[11] A. Schmeller, W. Hansen, J. P. Kotthaus, G. Tränkle, and G. Weimann, "Franz-Keldysh Effect in a Two-dimensional system," Appl. Phys. Lett. **64**, 330 (1994).

[12] A. Mysyrowicz, D. Hulin, A. Antonetti, A. Migus, W. T. Masselink, and H. Morkoç, ""Dressed Excitons" in a Multiple-Quantum Well Structure: Evidence for an Optical Stark Effect with Femtosecond Response Time," Phys. Rev. Lett. **56**, 2748 (1986).

[13] P. Bucksbaum, "Introduction to the high intensity physics of atoms and free electrons," in: *Atoms in Strong Fields*, edited by C. A. Nicolaides *et al.* (Plenum Press, New York, 1990).

[14] K. Johnsen and A.-P. Jauho, "Quasienergy Spectroscopy of Excitons," Phys. Rev. Lett. **83**, 1207 (1999).

[15] Y. B. Zel'dovich, "The Quasienergy of a Quantum-Mechanical System Subjected to a Periodic Action," Sov. Phys. JETP **24**, 1006 (1967).

[16] K. Johnsen and A. P. Jauho, "Linear optical absorption of mesoscopic structures in intense THz fields: Free particle properties," Phys. Rev. B **57**, 8860 (1998).

[17] A. H. Chin, J. M. Bakker, and J. Kono, "Ultrafast Electroabsorption at the Transition between Classical and Quantum Response," Phys. Rev. Lett. **85**, 3293 (2000).

[18] K. B. Nordstrom, K. Johnsen, S. J. Allen, A.-P. Jauho, B. Birnir, J. Kono, T. Noda, H. Ariyama, and H. Sakaki, "Excitonic Dynamical Franz-Keldysh Effect," Phys. Rev. Lett. **81**, 457 (1998).

[19] J. Kono, M. Y. Su, T. Inoshita, T. Noda, M. S. Sherwin, S. J. Allen, and H. Sakaki, "Resonant Terahertz Optical Sideband Generation from Confined Magnetoexcitons," Phys. Rev. Lett. **79**, 1758 (1997).

[20] C. Phillips, M. Y. Su, M. S. Sherwin, J. Ko, and L. A. Coldren, "Generation of first-order terahertz optical sidebands in asymmetric coupled quantum wells," Appl. Phys. Lett. **75**, 2728 (1999).

[21] M. A. Zudov, J. Kono, A. P. Mitchell, and A. H. Chin, "Time-resolved, nonperturbative, and off-resonance generation of optical terahertz sidebands from bulk GaAs," Phys. Rev. B **64**, 121204(R) (2001).

[22] M. Y. Su, S. G. Carter, M. S. Sherwin, A. Huntington, and L. A. Coldren, "Strong-field terahertz optical mixing in excitons," Phys. Rev. B **67**, 125307 (2003).

[23] G. D. Reid and K. Wynne, *Encyclopedia of Analytical Chemistry* (John Wiley & Sons Ltd, Chichester, 2000).

[24] L. V. Keldysh, "Ionization in the Field of a Strong Electromagnetic Wave," Soviet Phys. JETP **20**, 1307 (1965).

[25] S. E. Harris, J. E. Field, and A. Imamoglu, "Nonlinear Optical Processes Using Electromagnetically Induced Transparency," Phys. Rev. Lett. **64**, 1107 (1990).

[26] J.-P. Laude, *DWDM: Fundamentals, Components and Applications* (Artech House, Boston, 2002).

[27] D. Nesset, T. Kelly, and D. Marcenac, "All-Optical Wavelength Conversion sing SOA Nonlinearities," IEEE Comm. Mag. **163**, 56 (December 1998).

[28] D. A. B. Miller, *Confined Electronics and Photons* (Plenum Press, New York, 1995).

[29] A. Neogi, T. Mozume, H. Yoshida, and O. Wada, "Intersubband Transitions at 1.3 and 1.55 μm in a Novel Coupled InGaAs-AlAsSb Double-Quantum-Well Structure," IEEE Photonics Tech. Lett. **11**, 632 (June 1999).

[30] S. Gupta, M. Y. Frankel, , J. A. Valdmanis, J. F. Whitaker, G. A. Mourou, F. W. Smith, and A. R. Calawa, "Subpicosecond carrier lifetime in GaAs grown by molecular beam epitaxy at low temperatures," Appl. Phys. Lett. **59**, 3276 (1991).

[31] M. Troccoli, C. Gmachl, F. Capasso, D. L. Sivco, and A. Y. Cho, "Mid-infrared ($\sim$ 7.4 μm) quantum cascade laser amplifier for high power single-mode emission and improved beam quality," Appl. Phys. Lett. **80**, 4103 (2002).

[32] M. Holthaus, "Collapse of minibands in far-infrared irradiated superlattices," Phys. Rev. Lett. **69**, 351 (1992).